Sphingosine-1-Phosphate Receptor 1 regulates competition dependent astrocyte morphogenesis and tiling in murine cortex.

Jean Patrick M. Gonzales[1*], Connor Tuck[1*], Surya Chandra Rao Thummu[1], Soha Munir[1], Jaden Harris[1], Hunain (Zeik) Tariq[1], Paul Marcelli[1], Oscar Dominguez[1], Kaviya Suriyakumar Anbazagan, and Sandeep K. Singh[1#]

[1]Department of Cellular, Molecular and Genetic Medicine, School of Medicine and the Massey Comprehensive Cancer Center, Virginia Commonwealth University, Richmond, Virginia, 23298, USA.

* These authors contributed equally.

Running title: S1PR1 regulates astrocyte Tiling

Address correspondence to: Dr. Sandeep K. Singh, Department of Cellular, Molecular, and Genetic Medicine, Virginia Commonwealth University, Richmond, VA 23298, tel. (804) 828-9725, fax. (804) 828-1473, email: Sandeep.Singh@vcuhealth.org

Abstract

Astrocytes are highly abundant in the mammalian brain and coordinate with neurons and other glial cells to regulate neural circuit structure, function, and blood brain barrier integrity among many to maintain proper brain homeostasis. Astrocytes perform most of these functions owing to their highly complex morphologies and hundreds of thousands of fine processes that are important in contacting neuronal synapses and other glial cells. In fact, the morphological complexity of astrocytes is regulated by the presence and activity of neurons and helps establish astrocyte territory/tiling in a non-overlapping pattern; however, the mechanisms of astrocyte tiling are not well characterized. Using a human astrocyte-mouse neuron coculture system, we previously showed that sphingosine-1-phosphate receptor 1 (S1PR1) regulates astrocyte morphogenesis in a neuronal contact dependent manner. In this study, we find that S1PR1, *in vivo,* regulates astrocyte morphogenesis in a cortical layer specific manner. Using astrocyte-specific S1PR1 knock out mouse models and adenoassociated viral labeling methods, we show that S1PR1 is crucial in establishing competition driven astrocyte tiling and morphogenesis in the developing brain. Furthermore, we show that JAK-STAT3 signaling regulates neuronal contact induced expression of S1PR1 in cocultured astrocytes. These studies therefore uncover a lipid signaling receptor as a major regulator of astrocyte morphogenesis and tiling in murine cortical layers.

Introduction

Development of the central nervous system (CNS) is stringently coordinated and regulated by intricate physical, biochemical, and spatiotemporal modes of cross-communication between nervous system cells. Within the brain, cells form dynamic and functional neural-glial networks through the integration of cell-cell interactions, growth factor signaling, and neural activity, which culminate in the activation of neurogenic, downstream intracellular signaling cascades. These interconnected networks provide the structural and functional foundation for higher-order brain processes—including cognition, learning and memory, perception, and emotion—facilitating swift processing of information to adapt to changes in environmental stimuli. Improper assembly of neural-glial networks is a characteristic feature of numerous neurodevelopmental and neurological disorders, including Autism and Alzheimer's disease, highlighting the importance of understanding the key players and molecular mechanisms that govern this process[1–3].

Astrocytes are one of the key players participating in neural-glial networks and are a versatile cell type in the mammalian brain[4,5] Defined by their highly polarized and elaborate morphology, astrocytes extend ramified processes into the surrounding parenchyma to directly contact or come into proximity with neighboring neurons, glia, and vasculature[6]. These processes serve as an interface for intercellular communication through which astrocytes perform a range of essential functions: they provide metabolic and trophic support to energy-demanding neurons[7], coordinate with microglia to remove cellular debris and prune excess synapses during development[8,9], facilitate oligodendrocyte-mediated myelination of axons[10], and establish non-overlapping domains by maintaining boundaries with adjacent astrocytes[11]. Although the molecular cues and intrinsic genetic programs governing astrocyte differentiation are well

61 characterized[12,13], the intercellular signaling events that guide astrocyte maturation and sculpt their
62 morphological complexity during postnatal brain development are not fully understood.

63 While protein-centric effectors and signaling pathways have been extensively studied in
64 the context of astrocyte differentiation and development[14,15], emerging evidence highlights the
65 critical contribution of lipids—particularly sphingolipids—in astrocyte biology. Sphingolipids are
66 a diverse class of bioactive lipids that are synthesized *de novo* through conserved, endoplasmic
67 reticulum-resident metabolic pathways and are enriched in the brain, where they serve both
68 structural and signaling roles[16]. In cellular membranes, sphingolipids help organize lipids into
69 microdomains, or "lipid rafts," which concentrate signaling complexes and regulate membrane
70 trafficking[17,18]. More importantly, many sphingolipid metabolites act as potent intracellular and
71 extracellular signaling molecules that influence cell survival, proliferation, differentiation, and
72 morphology[19]. Within the CNS, sphingolipids have well-documented roles in neuronal
73 development and synaptic transmission[20,21]; however, their functions in astrocytes remain less
74 defined. Recent studies suggest that sphingolipid metabolites, such as Sphingosine-1-Phosphate
75 (S1P), regulate astrocyte proliferation, migration, and morphological differentiation[22–24]. S1P,
76 acting through its G-protein-coupled receptors, can influence cytoskeletal dynamics to promote
77 process extension, a hallmark of astrocyte morphogenesis[25–27]. In addition, altered levels of S1P
78 and genes within the S1P metabolic pathway are altered in many neuropathologies, including
79 Parkinson's disease, Alzheimer's disease, and neuropathic pain; yet the fundamental role of the
80 S1P-S1PR1 axis in the brain remains less explored.

81 Previously, we've shown that the expression of the G-protein-coupled receptor S1PR1
82 increases during postnatal brain development in mice and is primarily localized to perisynaptic
83 astrocytic processes (PAPs) and regulates astrocyte morphogenesis in a neuronal contact-

84 dependent manner. Furthermore, exogenous S1P led to a marked increase in astrocyte complexity
85 and expression of genes encoding astrocyte-secreted synaptogenic factors (SPARCL1 and TSP4)
86 when cocultured with neurons. These findings suggest that the S1P–S1PR1 signaling axis
87 modulates neuron-astrocyte interactions in promoting astrocyte morphological maturation and
88 their synapse association[28]. More recently, *in vivo* studies using *drosophila* (invertebrate) and
89 zebrafish (vertebrate) models have further substantiated the role of S1P–S1PR1 signaling in
90 astrocyte morphogenesis. The astrocyte-specific deletion of S1PR1 in zebrafish, or its functional
91 homolog Tre1 in Drosophila, resulted in significantly reduced astrocyte volume and branching
92 complexity[29]. However, the role of S1P-S1PR1 signaling in higher-order, mammalian astrocytes
93 has yet to be elucidated.

94 In this study, we investigated the role of S1PR1 in regulating astrocyte morphogenesis
95 during murine postnatal brain development. Our findings demonstrate that S1PR1 modulates
96 murine astrocyte size, branching complexity, and territorial tiling in a cortical layer-specific
97 manner. In addition, our *in vitro* astrocyte-neuron coculture experiments identified the JAK/STAT3
98 signaling pathway as a regulator of neuronal contact-dependent expression of S1PR1 in astrocytes.
99 Together, these findings position S1P-S1PR1 signaling as a novel regulator of murine astrocyte
100 development in a local neuronal signaling-driven manner, underscoring its importance in
101 establishing the complex morphology required for astrocyte function and overall brain
102 homeostasis.

103 **Materials and Methods**

104 ***Mice***

105 All mice used in this study were maintained on a C57BL/6J background. Knockout mice
106 were generated by crossing S1PR1$^{loxP/loxP}$ (a gift from Dr. Laura Sim-Selley, VCU) mice with
107 GFAP-Cre mice (JAX, #024098). To label astrocytes and their processes, we intracranially injected
108 either AAV pZac2.1-GfaABC1D-YFP, AAV pZac2.1-GfABC1D-Lck-GFP, AAV pZac2.1-
109 GfABC1D-YFP-P2A-Cre, AAV pZac2.1-GfaABC1D-tdTomato, or AAV pZac2.1-GfaABC1D-
110 tdTomato-P2A-Cre in P2-P3 pups. Four weeks after injection, the mouse brains were collected and
111 S1PR1 expression was confirmed via immunofluorescence staining. Afterwards, astrocyte
112 morphological imaging and analysis was performed. To determine the cell-type specificity of the
113 GFAP-Cre mouse line, we crossed unfloxed GFAP-Cre mice with the B6J.129(B6N)-
114 Gt(ROSA)26Sor$^{tm1(CAG-cas9*,-EGFP)Fezh/}$J (or Rosa26 loxP-STOP-loxP Cas9-P2A-GFP mouse (JAX
115 # 021675)) to generate a Cre-dependent reporter mouse. In this line, Cas9 and GFP expression is
116 limited to cells expressing Cre thereby allowing to report specificity and efficiency of GFAP-Cre
117 promoter. For *in vitro* experiments, P1 and P3 animals were used for neuronal and astrocyte
118 cultures, respectively. The above experiments were approved by Virginia Commonwealth
119 University IACUC.

120 ***Primary neuron isolation***

121 Mouse cortical neurons were isolated from wild-type C57BL/6 P1 pups as described
122 earlier[30]. Briefly, the cortices were dissected and digested with papain (Worthington Biochemical
123 Corp) in the presence of DNase at 36°C for 45 mins (with intermittent swirling every 15 mins),
124 followed by trituration in low and high concentrations of ovomucoid. The cells were passed
125 through 40 µm nitex filters (Fisher Scientific) and subjected to a series of negative panning plates
126 coated with 2× Bandeiraea Simplicifolia Lectin I (Vector Laboratories) followed by incubation at
127 room temperature (RT) in AffiniPure goat anti-mouse IgG + IgM (H + L) (Jackson

128 Immunoresearch Laboratories, PA) and anti-neural cell adhesion molecule L1 (MAB5272,
129 Millipore) coated positive panning dishes to obtain >95% pure cortical neurons. Following
130 incubation, the cells were collected, centrifuged at 1100 rpm for 15 mins, and resuspended in
131 neurobasal growth medium (NGM) comprised of neurobasal medium, B27, 100 U/mL Pen/Strep,
132 2 mM L-Glutamine, and 1 mM Na+Pyruvate. All the media components were procured from Gibco
133 unless otherwise stated. The cells were counted and seeded onto poly-D-lysine (PDL)/laminin-
134 coated coverslips at a density of 2 x 10^5 cells per coverslip in a 24-well plate and incubated in a
135 humidified chamber with 10% CO_2 at 37°C. AraC (1 uM) was added onto the wells for the initial
136 24-36 h to prevent the growth of glial cells. Every 3 days, half of the neurobasal medium was
137 replaced with fresh medium until the day of the experiments.

138 ***Astrocyte isolation from S1PR1-GFP mouse brain***

139 *S1pr1*$^{eGFP/eGFP}$ (B6.129P2-S1pr1tm1Hrose/J)(JAX # 028623) mouse cortical astrocytes
140 were obtained from newborn pups (P3) as described earlier[30] with slight modifications. Briefly,
141 the cortices from the pups were dissected and the tissue was digested with papain in the presence
142 of DNase at 36° C for 45 minutes. Papain-digested tissue was triturated with low and high
143 ovomucoid solutions, filtered through nitex mesh (20 µm), and resuspended in serum free
144 neurobasal growth medium (exactly as was for neurons). The cells were counted using an
145 automated cell counter, and 10-14 million cells were plated in 75 cm^2 flasks coated with poly-D-
146 lysine and incubated at 37°C in 10% CO_2. On DIV-3, neurobasal medium was removed and rinsed
147 with DPBS (-$MgCl_2$ and -$CaCl_2$) and shaken by hand for 10–15 seconds or until a monolayer of
148 astrocytes remained. The cells were rinsed once with DPBS (-$MgCl_2$ and -$CaCl_2$) and replenished
149 with fresh medium. Upon confluency (typically around DIV6-7), astrocytes were trypsinized with

150 0.25% trypsin and passaged to 6-well dishes with 7-8 x 10^5 cells per well and maintained till around
151 DIV10.

152 ***Neuron-astrocyte coculture experiments***

153 For neuron-astrocyte co-culture experiments, the astrocytes cultured from S1PR1-GFP
154 pups at around DIV8-DIV10 were detached with 0.25% trypsin following which trypsin was
155 neutralized using DMEM containing 10% FBS medium. The cells were triturated to create a
156 single-cell suspension, centrifuged at 200g for 11 minutes, and resuspended in neuronal growth
157 medium; cell counts were taken, and ~3 x 10^4 cells were added to each well of a 24 well plate
158 containing WT neurons. Separate wells were maintained where only astrocytes were added to the
159 coverslips coated with PDL and laminin that served as astrocyte monoculture/control. Following
160 incubation in the presence and absence of neurons, the cells were fixed with 4% PFA.

161 ***Inhibitor treatment of neuron-astrocyte co-cultures***

162 For experiments investigating the role of signaling pathways such as JAK-STAT, Sonic
163 Hedgehog, and S1P-S1PR1 interaction in regulating astrocyte morphology and S1PR1 expression,
164 astrocyte monocultures or neuron-astrocyte co-cultures were treated with different inhibitors such
165 Ruxolitinib (1 μM), Sonidegib (5 μM), and W146 (200 nM), respectively. Inhibitors or vehicle
166 (DMSO) control was added to respective wells 30 min. prior to adding astrocytes into the wells
167 with or without DIV7-9 neurons. In tandem with co-culture experiments, astrocyte monocultures
168 were treated with inhibitors along a similar timeline. Twenty-four-hour post incubation, cells were
169 fixed, immunostained, and imaged for analysis.

170 ***Immunofluorescence analysis of frozen brain tissues***

171 Mice were anesthetized using isoflurane inhalation and transcardially perfused with 1×
172 PBS pH 7.4 followed by 4% paraformaldehyde. Brains were harvested, fixed in 4%
173 paraformaldehyde overnight, and placed in 30% sucrose for 48-72 h before being embedded in a
174 2:1 30% sucrose:OCT solution. Coronal brain slices of 50 µm (morphological analyses using YFP
175 or Lck-GFP labelling) and 20 µm (immunofluorescence analyses) were cryosectioned on a
176 cryostat, rehydrated in 1× PBS for 15 min, blocked with 10% goat serum in PBS with 0.5% Triton
177 x-100 for 1 hour, primary antibody incubation overnight at 4°C, followed by a 2 hour secondary
178 antibody incubation at RT, and mounted using VECTASHIELD Antifade Mounting Media with
179 DAPI (Vector Laboratories, H-1000). The following primary antibodies were used: Mouse anti-
180 GFAP (1:500; Cell Signaling Technology, 3670S), Rat anti-CD31 (1:200; Abcam, ab56299),
181 Rabbit anti-AQP4 (1:500; Alomone, AQP-014), Rabbit anti-S1PR1 (1:100; Santa Cruz, sc-48356),
182 Guinea pig anti-GLT1 (1:500; EMD Millipore, AB1783), Rabbit anti-NeuN (1:500; Cell Signaling
183 #24307), Rabbit Iba1 (1:1000; Wako Corporation #019-19741), Chicken anti-OLIG2 (1:500;
184 Antibodies Incorporated # OLIG2-0100), Rabbit anti-SOX9 (1:500; Cell Signaling; #82630) and
185 Chicken anti-GFP (1:1000; Aves; # GFP-1010) . The following secondary antibodies were used:
186 Alexa Fluor 594 goat anti-rat (1:200; Thermo Fisher Scientific, A11007), Alexa Fluor 488 goat
187 anti-rabbit (1:500; Thermo Fisher Scientific, A11034), Alexa Fluor 488 goat anti-Mouse (1:500;
188 Thermo Fischer Scientific, A32723), Alexa Fluor 594 goat anti-Guinea pig (1:500; Thermo Fischer
189 Scientific, A11076), and Alexa Fluor 488 goat anti-Chicken (1:500; Thermo Fisher Scientific
190 #A32931TR).

191 ***Immunofluorescence analysis of astrocyte-neuron cocultures***

192 For immunostaining, cells were fixed in 4% paraformaldehyde (PFA) at room temperature
193 for 10 minutes. Following fixation, cells were rinsed with 1x PBS twice at room temperature (RT),

194 followed by blocking with blocking buffer containing 50% Normal Goat Serum (NGS) and 0.2%
195 Triton-X100 in antibody solution. Cells were then incubated in antibody solution with 10% NGS
196 overnight at 4°C with the following antibodies: anti-GFP (1:2000, Aves; # GFP-1010), anti-S100b
197 (1:500, Millipore) and anti-Map2 (1:2000, Cell Signaling; #8707). Subsequently, the cells were
198 washed 3x with 1X PBS and incubated with species-specific secondary antibodies conjugated with
199 Alexa Fluor 488 (1:500) or Alexa Fluor 594 (1:500) in an antibody solution with 10% NGS for 1h
200 at RT. Coverslips were then washed three times with 1X PBS and mounted with VECTASHIELD
201 Antifade Mounting Media (Vector Laboratories, H-1000). Cells were imaged at 20x magnification
202 using a confocal microscope (Zeiss LSM 710).

203 ***Confocal Imaging and Image analysis***

204 For analysis of astrocyte morphology *in vitro*, GFP signals from astrocytes were used for
205 measuring complexity using the Sholl analysis plugin in FIJI. Briefly, images were smoothened
206 (process-smooth) and converted to a binary signal. The freehand tool was used to generate a region
207 of interest (ROI) around the astrocyte and remove processes from neighboring cells. Using the
208 straight, segmented, or freehand lines tool, an ROI was marked at the center of the cell and
209 stretched to the longest processes of the astrocyte, followed by execution of Sholl analysis
210 (Plugins-neuroanatomy-Sholl-Sholl analysis). For measurement of the intensity, area, and
211 perimeter of individual astrocytes, the green channel was converted to a grayscale image, followed
212 by threshold adjustment, which was set the same for all the images. Using the wand tracing tool,
213 each cell was selected and measured. To evaluate astrocyte morphology *in vivo*, fluorescence
214 images were acquired using the Zeiss LSM 880 laser-scanning confocal microscope with a ×40
215 oil-immersion objective with a frame size of 1,024 × 1,024 and bit depth of 16 (Zen3.1). Serial
216 images at the z-axis were taken at an optical step of 0.5 um, with the overall *z*-axis range

217 encompassing entire astrocytes. Images were imported into Imaris Bitplane software, and only
218 astrocytes with their soma between the *z*-axis range were chosen for further analysis. We performed
219 3D surface rendering using the Imaris Surface module to characterize astrocyte volume and surface
220 area. Morphological analysis was performed using the Imaris Filament module. Astrocyte
221 branches and processes were outlined by Autopath with the starting point set at 8 μm and the seed
222 point set at 0.5 μm, and statistical outputs, including 'filament number Sholl intersections,' were
223 extracted and plotted with Prism software. To analyze the knockout efficiency of *S1PR1*,
224 fluorescence images were acquired using a Zeiss LSM 880 laser-scanning confocal microscope
225 with a 20x objective. To measure the fluorescence intensity of GFAP and AQP4 fluorescence
226 images were acquired using the Keyence BZ-X1000 fluorescence microscope with a 20x objective
227 and analyzed using Fiji. GLT1 images were acquired at 63X magnification in Zeiss 880 confocal
228 microscope and analyzed using Fiji. Brains from the GFAP-Cre Cas9 reporter mice were stained
229 and imaged for NeuN, Iba1, OLIG2, GFAP and GFP using a Zeiss LSM 880 laser-scanning
230 confocal microscope with a 20x objective. The person who analyzed the images was blinded to
231 the experimental groups.

232 ***Tracer dye experiment to measure Blood-Brain Barrier Integrity***

233 Brain tracer leakage experiments were performed as described[27,28]. Mice (4-5 wk of age)
234 were injected in the tail vein with Alexa Fluor 555–cadaverine (6 μg/g; Invitrogen) or 3-kDa
235 dextran–TMR (10 μg/g; Invitrogen) dissolved in saline. After 2 h (for Alexa Fluor 555–cadaverine
236 or 3-kDa dextran–TMR) mice were anesthetized and perfused for 7 min with ice-cold PBS (pH
237 7.4), and brains were removed. After dissection, the cortex was weighed and homogenized with
238 1% Triton X-100 in PBS. Cortical lysates were centrifuged at 12,000 × *g* for 20 min at 4°C, and

239 the supernatant was used to quantify fluorescence (excitation/emission 540/590 nm; SpectraMax
240 M2e; Molecular Devices). The relative fluorescence values were normalized with cortical weights.

241 ***AAV packaging***

242 All AAVs used in this study were produced in the Singh lab unless otherwise mentioned,
243 in accordance with the US National Institutes of Health Guidelines for Research Involving
244 Recombinant DNA Molecules and the Virginia Commonwealth University Institutional Biosafety
245 Committee. pAAV-GfaBC1D-YFP-P2A-Cre plasmid was created by subcloning P2A-Cre from
246 pAAV-hSynapsin-mCherry-P2A-Cre-WPRE plasmid (a gift from Hui Yang (Addgene plasmid #
247 107312); into the pAAV-GfaBC1D-YFP plasmid. Similarly, pAAV-GfaBC1D-tdTomato and
248 pAAV-GfaBC1D-tdTomato-P2A-Cre was created by subcloning and replacing YFP with that of
249 tdTomato into pAAV-GfaBC1D-YFP or pAAV-GfaBC1D-YFP-P2A-Cre plasmid respectively.
250 The serotype AAV plasmid, PHP.eB (pUCmini-iCAP-PHP.eB), was a gift from Viviana Gradinaru
251 (Addgene plasmid #103005; RRID: Addgene_103005). pAAV.GfaBC1D-PI-Lck-GFP-SV40 was
252 a gift from Baljit Khakh (Addgene viral prep # 105598-AAV5).

253 AAV packaging was performed as previously described[31]. Briefly, ~$1x10^8$ HEK293T cells
254 (ATCC #CRL 3216) grown in 6, T-175 flasks were transfected using polyethylenimine (PEI) with
255 the pAAV of choice, the helper plasmid pAd-ΔF6 (Addgene Plasmid (#112867), and the serotype
256 plasmid AAV PHP.eB at a ratio of 1:1:2 using polyethylenimine transfection. The media was
257 changed the following day, and cells were cultured for an additional 48 hours. After 72 hours post-
258 transfection, cells were scraped, pelleted, resuspended in cell lysis buffer (15mM NaCl, 5mM Tris-
259 HCl, pH 8.5), followed by 3, 10-minute freeze-thaw in a dry ice/ethanol bath followed by a 37° C
260 water bath. Cell lysates were treated and incubated at 37°C with benzonase (50 U/ml) for 30
261 minutes and centrifuged at 4500 rcf for 30 min at 4°C to collect the supernatant. The supernatant

262 was added to a 15%, 25%, 40%, and 60% iodixanol gradient loaded into a polypropylene
263 ultracentrifuge tube (~1% phenol red was incorporated into the 25% and 60% layer to visualize
264 the density gradient), and underwent ultracentrifugation at 67,000 rpm using a Beckman Ti-70
265 rotor for 1 hour at 18 °C. After ultracentrifugation, the AAV fraction was collected using a syringe
266 with an 18 G needle and concentrated with four washes of DPBS (Millipore, 100 K MW) via
267 centrifugation at 4000 × *g* for 10 minutes each. A final volume of 200 µl of virus after the final
268 buffer exchange was recovered from the column, aliquoted and stored at -80°C.

269 ***Intracranial injection of AAV viruses***

270 For astrocyte labeling, we utilized pAAV-GfaABC1D-YFP, pAAV-GfaBC1D-Lck-GFP,
271 pAAV.GfaBC1D-YFP-P2A-Cre (sparse KO), pAAV-GfaBC1D-tdTomato, and pAAV-GfaBC1D-
272 tdTomato-P2A-Cre (Territory overlap). In brief, pups aged post-natal days 2-3 were anesthetized
273 on ice, followed by a 0.8 µL viral injection (~1x 10^9 virus particles) using a Hamilton neurosyringe
274 microinjector at a depth of 0.5 mm in the right hemisphere of the visual cortex. After injections,
275 pups were gently placed on a heating pad to recover and closely monitored. All of the animal
276 procedures were performed in accordance with approved VCU IACUC protocols.

277 ***Astrocyte territory overlap/tiling analysis***

278 P3 S1PR1$^{f/f}$ pups were intracranially injected with 1 µL of a combination of control AAVs
279 (GfaABC1D-YFP + GfaABC1D-tdTomato) or Cre AAVs (GfaABC1D-YFP-P2A-Cre +
280 GfaABC1D-tdTomato-P2A-Cre) mixed at a 1:1 ratio, respectively. At P30, the mouse brains were
281 collected, cryosectioned, and 50 µm Z-stack (0.5 µm Z-intervals) images which contained two
282 neighboring astrocytes (expressing either YFP or tdTomato) were collected. Astrocytes containing
283 endfeet were excluded from this experiment.

284 IMARIS 11 was used to generate a 3D surface reconstruction of the YFP and tdTomato astrocyte
285 to generate fluorescent channel masks of each astrocyte. Filament traces were then generated from
286 each astrocyte to utilize the "Convex Hull" Imaris Xtension to generate a surface representing the
287 territory of each astrocyte. Territory overlap was measured by creating a mask of the original
288 fluorescent channel within the convex hull, and the colocalization tool in Imaris was used to
289 generate a colocalization channel representing territory overlap between the masked YFP and
290 tdTomato channels. Then, a surface of the colocalization fluorescent channel was generated to
291 record the volume of territory overlap. Territory overlap volume measurements were normalized
292 to the territory volume of both the YFP (green) and tdTomato (magenta) astrocyte to control for
293 variations in the astrocyte size, as the 50 µm Z-stack limitation prevented capture of at least one
294 astrocyte in its entirety.

295 ***Quantification and statistical analysis***

296 Sample sizes and statistical tests can be found in the accompanying figure legends. Offline
297 analysis was performed using Graphpad Prism 11 and Microsoft Excel. Statistical significance was
298 determined by unpaired 2-tailed Welch's t-tests for comparison of 2 groups. Data are presented as
299 mean ± s.e.m. Statistical significance is indicated by asterisks: $*P < 0.05$, $**P < 0.01$,
300 $***P < 0.001$, $****P < 0.0001$. The number of independent experiments (n) and the number of
301 analyzed cells is noted in the figure legends.

302

303 **Results**

304 **Astrocyte morphology and S1PR1 expression are driven by neuronal contact *in vitro*.**

305 We have previously demonstrated that the expression of S1PR1 in the developing mouse
306 brain coincides with synaptogenesis and the maturation of astrocytes, and that neuronal contact
307 stimulates S1PR1 expression in astrocytes[28]. To further investigate S1PR1's expression and
308 localization dynamics, we prepared primary astrocyte cultures from S1PR1 reporter mice
309 ($S1PR1^{GFP/GFP}$) (JAX Strain # 028623) in serum-free medium. It is well established that astrocytes
310 cultured in the presence of serum can adopt a reactive phenotype and exhibit altered morphology
311 and gene expression[32]. To avoid these confounding effects, our astrocytes were maintained in
312 serum-free Neurobasal medium, and we verified the cellular purity of these cultures (Fig. S1 and
313 data not shown). We validated S1PR1 expression by probing for GFP in astrocytes marked with
314 S100b and found that S1PR1 signal primarily localizes to astrocytic plasma membranes (Fig. S1B).
315 Therefore, we can simultaneously measure S1PR1 expression (quantified as GFP fluorescent
316 intensity) and astrocyte morphological parameters (perimeter and Sholl analyses) using GFP
317 signal. S1PR1-GFP astrocytes cultured alone exhibit a simple, flattened fibroblast-like
318 morphology and basal S1PR1 signal. Interestingly, most astrocytes cocultured with neurons exhibit
319 increased S1PR1 expression, three-dimensionality, and extensive branching (Fig. S1B,C);
320 however, some astrocytes still maintained a simple morphological state with low S1PR1 signal
321 (Fig. S1C). To determine whether neuronal contact induces S1PR1-GFP expression and drives
322 astrocyte complexity, S1PR1-GFP astrocyte/WT neuron cocultures were immunostained with the
323 neuronal marker, MAP2 (Fig. 1A,E). This approach allowed us to identify neuronal processes and
324 explicitly measure astrocytes in direct contact (termed interacting astrocytes, or IA) versus no
325 contact with neurons (termed non-interacting astrocytes, or NIA) (Fig. 1A,E). Indeed, S1PR1-GFP

326 astrocytes in direct contact with MAP2^{+} neurons exhibited much higher S1PR1-GFP fluorescent
327 intensity and branching, as indicated by Sholl analyses (Fig. 1D,H) and increased perimeter (Fig.
328 1C,F) compared to astrocytes with no neuronal contact. Time course experiments also demonstrate
329 that the neuronal contact-dependent increase in S1PR1 expression and astrocyte complexity
330 already begins to show at 8 hours (Fig. 1A-D) and increases further at 24 hours (Fig. 1E-H).
331 Therefore, we provide evidence that neuronal contact directly and simultaneously induces S1PR1
332 expression and astrocyte morphological complexity. To further test the role of S1PR1 signaling in
333 contact-dependent astrocyte morphological complexity, we applied the S1PR1-specific antagonist,
334 W146[31] in these astrocyte-neuron cocultures and analyzed the astrocyte only conditions or IAs
335 (Fig. 1I,K). As expected, W146 significantly reduced neuronal contact-dependent astrocyte
336 complexity as measured by a reduction in perimeter (Fig. 1J) and number of Sholl intersections
337 (Fig. 1L), affirming the role of S1P-S1PR1 signaling in astrocyte morphogenesis. To our surprise
338 we also found that W146 significantly reduced neuronal-contact-induced expression of S1PR1 in
339 astrocytes (fig. 1K) but had no effect on astrocyte only cultures (Fig. 1K), further suggesting
340 S1PR1 signaling may also self-regulate its expression in astrocytes when in contact with neuron.

341 Next, we sought to identify signals that induce expression of S1PR1 in astrocytes and thus in turn
342 regulate astrocyte morphogenesis. Several signaling pathways, including JAK-STAT3 and SHH-
343 GLI1, have been shown to play crucial roles in neuron-astrocyte interactions and modulate
344 astrocyte maturation and morphological complexity[32–34]. Therefore, we applied chemical
345 inhibitors of these pathways, Ruxolitinib and Sonidegib, respectively, to our coculture paradigm
346 (Fig. 2). Interestingly, while Ruxolitinib and Sonidegib both inhibited astrocyte morphological
347 complexity (Fig. 2B,D,E), neuronal contact induced expression of S1PR1 was significantly
348 inhibited by only Ruxolitinib in cocultures (Fig. 2C). These results demonstrate JAK-STAT3

349 signaling but not SHH signaling mediates neuronal contact-dependent expression of S1PR1 in
350 cocultured astrocytes.

351 **Astrocyte-specific S1PR1 knock-out mice exhibit no gross changes in blood vasculature,**
352 **astrocyte maturation and astrocyte numbers.**

353 To characterize the role of astrocytic S1PR1 in the developing brain *in vivo*, we generated
354 an astrocyte-specific S1PR1 knockout mouse line (termed $S1PR1^{\Delta AST}$) in which the S1PR1 gene
355 is exclusively deleted in astrocytes by crossing $S1PR1^{loxP/loxP}$ mice with the GFAP-Cre (77.6)
356 mouse line (Fig. 3A). S1PR1 expression at the mRNA level was drastically reduced in the cortices
357 of $S1PR1^{\Delta AST}$ mice at P30 compared to littermate controls (Fig. 3B), demonstrating astrocytes as
358 the major source of S1PR1 in the brain *in vivo*. We further performed immunofluorescence staining
359 and confocal imaging of S1PR1 in the cortices of $S1PR1^{\Delta AST}$ and littermate controls and found
360 strong expression of S1PR1 within the cortex of control brains and a drastically reduced signal in
361 $S1PR1^{\Delta AST}$ cortices (Fig. 3C). Interestingly, endothelial S1PR1 expression remained unchanged in
362 $S1PR1^{\Delta AST}$, as evidenced by colocalization of the endothelial cell marker, CD31, with S1PR1 (Fig.
363 3C, arrow). This observation is in line with the well-known expression of S1PR1 in endothelial
364 cells and is crucial for vascularization and maintenance of blood-brain barrier (BBB) integrity[35].
365 Because S1PR1 is expressed on astrocytic endfeet[28] and astrocyte endfeet are crucial in
366 maintaining BBB integrity, we investigated whether astrocytic S1PR1 may also participate in BBB
367 integrity and astrocyte-vasculature interactions. We immunostained $S1PR1^{\Delta AST}$or littermate
368 control brains at P30 with the astrocyte endfeet marker, AQP4, and endothelial cell marker CD31
369 (Fig. 3D,E) and observed no significant changes in the signal corresponding to the area and
370 fluorescent intensity of both AQP4 and CD31, implicating that astrocytic S1PR1 does not affect
371 the general structure of vasculature and endfeet (Fig. 2C-E). To conclusively demonstrate

372 astrocytic S1PR1's role in the functional maintenance of BBB integrity, we performed dye tracer
373 leakage experiments, which are well-established methods to measure BBB leakage[35]. In this assay,
374 we intravenously injected two tracer dyes, either a 3-kDa dextran or the smaller 1-kDa cadaverine,
375 and measured their relative accumulation in the brain tissue (Fig. 3F). Leakage of both tracer dyes
376 was comparable between cohorts (Fig. 3F), suggesting that astrocytic S1PR1 does not play a
377 prominent role in BBB integrity.

378 Since S1P signaling modulates cell growth and proliferation and that S1PR1 is expressed
379 during astrocyte development, we measured astrocyte-cell numbers in the cortices of P30
380 S1PR1$^{\Delta AST}$ by immunostaining for SOX9 and OLIG2 and counting SOX9+OLIG2- nuclei as
381 astrocytes as previously reported[38](Fig. S2). No apparent difference in the number of
382 SOX9+OLIG2- cells were observed between control and KO, indicating that astrocyte number
383 was unaltered (Fig. S2B). Additionally, we measured the maturation and reactivity status of
384 astrocytes in S1PR1$^{\Delta AST}$ mice by immunostaining for GFAP and observed no change in either
385 fluorescent intensity or GFAP structure in the cortex (Fig. 3G). We have previously demonstrated
386 that S1PR1 is highly expressed on perisynaptic astrocyte processes (PAPs) and strongly colocalizes
387 with PAP marker, GLT1 (SLC1A2; glutamate transporter encoded by the gene *Slc1a2*), in the
388 developing brain[28]. Therefore, we immunostained, imaged and quantified GLT1 puncta (or "spot")
389 count and spot volume using IMARIS 3D rendering to generate GLT1 spots from S1PR1$^{\Delta AST}$
390 brains (Fig. 3H). We observed no significant difference in the number or size of GLT1 spots in
391 astrocytes between S1PR1$^{\Delta AST}$ or littermate controls (Fig 3H), suggesting that the loss of astrocytic
392 S1PR1 does not alter GLT1 expression or GLT1 containing PAPs.

393 **S1PR1 KO astrocytes exhibit altered morphology and complexity *in vivo*.**

394 Because S1PR1 regulates neuronal contact-induced astrocyte morphogenesis *in vitro* (Fig.
395 1)[28], we asked whether astrocyte morphogenesis is also impacted *in* vivo during postnatal
396 development after loss of astrocytic S1PR1. We used an adeno-associated virus (AAV)-based
397 approach to sparsely label and cytosolically fill cortical astrocytes with YFP in S1PR1$^{\Delta AST}$ mice
398 (Fig. 4A). Briefly, P2-P3 S1PR1$^{\Delta AST}$ or littermate control pups were intracranially injected directly
399 into the cortex with the AAV, pZac2.1-GfaABC$_1$D-YFP, and brains were collected at P30, a
400 timepoint where most astrocyte proliferation and maturation have completed in mice (Fig. 4A).
401 Since astrocytes exhibit highly branched fine processes, 50 µm confocal Z-stacks of individual
402 astrocytes were imaged and 3D reconstructed using IMARIS to generate surface and filament
403 renderings for analysis (Fig. 4B).

404 Astrocytes are both functionally and structurally heterogeneous depending on brain region, neural
405 input, and cell-cell interactions[4,11]. The cortex can be subdivided into different functional layers
406 based on synaptic inputs and cytoarchitecture and contains diverse subpopulations of astrocytes
407 that have been extensively characterized[36]. Therefore, we decided to focus our studies on the upper
408 (L2-3) and deeper (L4-5) layer cortical astrocytes *in vivo*. Moreover, we chose the somatosensory
409 cortex (SSC) for our analyses because a) SSC astrocytes are shown to modulate peripheral
410 neuropathic pain and astrocytic S1PR1 is also crucial for neuropathic pain[37–39] and b) to avoid
411 potential injury-induced effects on astrocytes at the injection site in the visual cortex. In the
412 absence of S1PR1, L2-3 astrocytes had larger territories as defined by their total volume, soma
413 volume and territory volume (Fig. 4C,D), suggesting that S1PR1 limits astrocyte territory
414 formation. Next, we performed filament tracing analyses on these astrocytes to precisely determine
415 various parameters of their processes (branches) (Fig. 4D). S1PR1$^{\Delta AST}$ astrocytes showed no

416 changes in total filament length nor total filament area (Fig. 4D). Further, analyses of astrocyte
417 processes/filaments based on their thickness and grouped as a percentage of the total filament
418 distribution (Fig. 4F) did not reveal any differences regarding the proportion of thicker (likely main
419 processes) to thinner (distal processes or leaflets) processes per astrocyte (Fig. 4E). Although these
420 results clearly demonstrate overall larger astrocyte territory without changes in processes
421 parameters in S1PR1$^{\Delta AST}$, these analyses still do not show morphological differences in relation to
422 the astrocyte soma. Therefore, we utilized three-dimensional Sholl analysis on the filament
423 tracings to precisely plot astrocytic branch points (or intersections) in relation to the center of the
424 astrocyte soma (Fig. 4F). S1PR1$^{\Delta AST}$ astrocytes displayed significantly larger intersections beyond
425 20 μm from the center, indicating increased branching in distal processes (Fig. 4F, right panel).
426 Taken together, these results demonstrated that upper-layer cortical astrocytes are significantly
427 larger in S1PR1$^{\Delta AST}$. Additionally, larger astrocytes are not due to a decrease in total number of
428 astrocytes in S1PR1$^{\Delta AST}$ mice since quantification of astrocyte numbers (Sox9+Olig2-) in the
429 cortical layers revealed no apparent change (Fig. S2).

430 Next, we performed identical analyses from deeper cortical layer (layers 4-5) astrocytes from
431 S1PR1$^{\Delta AST}$ at P30 (Fig. 5A,B). Unlike astrocytes within upper layers of the cortex, deletion of
432 S1PR1 had no major effect on L4-5 astrocyte size or territory (Fig. 5C, 5D). The total astrocyte
433 volume, soma volume and territory volumes remained unchanged between cohorts (Fig. 5C, 5D)
434 as did the average total filament area and filament length (Fig. 5D); however, Sholl analyses
435 revealed a unique reduction in process branching between 20-40 μm away from the center of the
436 cell body (Fig. 5F, left panel) while no differences were observed in the processes near the cell
437 body and fine distal processes beyond 40 μm away, unlike in L2-3 astrocytes (Fig. 4F).
438 Furthermore, these L4-5 astrocytes did not show any change in the process size distribution (Fig.

439 5E). Taken together, we can conclude that S1PR1$^{\Delta AST}$ possesses layer-specific morphological
440 alterations.

441 **Membrane-tagged GFP filled S1PR1 KO astrocytes exhibit altered complexity *in vivo*.**

442 Astrocyte processes ramify into branches, branchlets, and leaflets, which contribute to 90–
443 95% of an astrocyte's total surface area and volume[11,40]. We reasoned that cytosolic GFP-labeling
444 may only define larger astrocyte processes and may not fully encapsulate the morphology or
445 territory occupied by a single astrocyte and its smaller/finer processes, and thus, may not detect
446 effects of S1PR1 in these finer processes. Therefore, we labeled astrocyte membranes via an AAV
447 mediated expression of Lck-GFP (pZac2.1 GfaABC$_1$D-Lck-GFP), a membrane-tagged GFP, in
448 S1PR1$^{\Delta AST}$ brains (Fig. S4) and performed the same analyses as in figures 4 and 5. Indeed, the
449 volume, surface area, and number of intersections in Lck-GFP astrocytes were approximately 2-
450 fold higher than that of cytosolic GFP filled astrocytes (compare Fig 4C and S4C) and are
451 comparable to previously reported values for cortical astrocytes[36]. Lck-GFP-labeled S1PR1$^{\Delta AST}$
452 astrocytes showed no significant changes in volumes and surface area in both the upper and deeper
453 cortical layers (Fig. S4 C,D and H,I). Sholl analyses of L2-3 Lck-GFP S1PR1$^{\Delta AST}$ astrocytes
454 showed an increase in the number of intersections at distances greater than 20 microns from the
455 cell body (Fig. S4E) while L4-5 Lck-GFP S1PR1$^{\Delta AST}$ astrocytes showed a significant decrease in
456 the number of intersections between 15-30 microns from the cell body (Fig. S4J) The Sholl
457 analyses are consistent between cytosolic YFP filled and membrane-tagged Lck-GFP experiments.
458 Taken together these results suggest an increased complexity in L2-3 and a decreased complexity
459 in L4-5 cortical astrocytes in S1PR1$^{\Delta AST}$ and overall reflect our initial observations in cytosolic
460 YFP-labeled astrocytes in earlier analyses (Fig. 4,5), further solidifying a layer-specific difference
461 in S1PR1-dependent astrocyte morphogenesis.

462 **Sparse knock-out of S1PR1 in the upper cortical layers reduces astrocyte morphology and**
463 **complexity.**

464 Global loss of astrocytic S1PR1 *in vivo* led to an increase in astrocyte morphological
465 complexity in the superficial layers (Fig. 4 and S4E), while there was a minor reduction in the
466 deeper layers (Fig. 5, S4J). Our findings are in direct opposition to our findings *in vitro* (Fig. 1)
467 and to those of others in the field studying invertebrate and zebrafish models[29]. We hypothesized
468 that our findings here may represent a unique complexity in mammalian models of astrocyte
469 morphology and, more specifically, astrocyte tiling. Although astrocyte tiling is conserved in
470 mammals, zebrafish, and Drosophila, the molecular mechanisms driving this phenomenon are less
471 known. It is, however, understood that astrocyte domains are established by repulsive or
472 competitive interactions between neighboring astrocytes[11]. Therefore, we hypothesized that
473 conditional loss of S1PR1 in the majority of astrocytes would lead to loss of competition-driven
474 tiling and extended astrocyte processes and territory volume. We predicted that a difference in
475 S1PR1 expression in neighboring astrocytes would result in reduced morphological complexity
476 and territory in the astrocytes with reduced S1PR1 expression (Fig. 6B). To test this possibility,
477 we simultaneously fluorescently labeled and sparsely deleted S1PR1 in cortical astrocytes by
478 injecting either the astrocyte-specific AAV pZac2.1 GfaABC1D-YFP-P2A-Cre or YFP as a control
479 into S1PR1$^{loxP/loxP}$ pups at P2-3 (Fig. 6A-C). We validated sparse S1PR1 knockout in YFP-P2A-
480 Cre expressing astrocytes at P30 and performed the exact same imaging parameters and
481 morphometric analyses as in Fig. 4,5.

482 Interestingly, individual S1PR1 KO (YFP-P2A-Cre injected) astrocytes in the upper layers
483 exhibited reduced astrocyte volume (Fig. 6D), territory volume (Fig. 6E), and a reduction in
484 complexity in the finer processes measured as number of intersections by Sholl (Fig. 6G) compared

485 to control astrocytes (YFP injected only). Additionally, we saw a significant reduction in filament
486 length and area (Fig. 6E) but no obvious change in filament diameter populations (Figs. 6F).
487 Collectively, these results indicate that sparse S1PR1 KO astrocytes are overall smaller and less
488 complex in the upper cortical layers. These results contradict our previous morphometric results
489 from S1PR1 deletion in a total astrocyte background (Figs. 4) but are in line with our prediction
490 that S1PR1 may play a role in competition-dependent astrocyte growth and tiling of the upper
491 cortical layers (Fig. 6B).

492 Next, we focused our analyses on deeper layer astrocytes in the sparse S1PR1 KO model
493 (Fig. 7A,B). Deletion of S1PR1 from individual astrocytes in the deeper layer showed a strong
494 reduction in overall astrocyte volume and territory volume compared to control astrocytes (Fig.
495 7C,D). Moreover, Sparse S1PR1 deletion from deeper layer astrocytes also exhibited a reduction
496 in the number of intersections compared to control (Fig. 7F); however, no significant redistribution
497 in process diameters or overall process length was observed (Fig. 7E). Since excessive Cre
498 expression may affect cellular health and affect astrocyte morphology even in the absence of a
499 floxed allele, we injected AAVs expressing YFP or YFP-P2A-Cre into C57BL/6J (wild-type) pups
500 at P2-3 and subsequently analyzed astrocyte morphology (Fig. S5). In our hand, Cre expression
501 alone did not cause any substantial changes in astrocyte volume, territory or branching (Fig. S5C-
502 E). Taken together, sparse S1PR1 KO astrocytes in deeper cortical layers showed an overall
503 reduced territory size and stronger reduction in complexity, suggesting a role of S1PR1 in
504 competition-driven astrocyte process growth and tiling.

505 **S1PR1 regulates astrocyte territorial overlap/tiling**

506 So far, our results indicate a role for astrocytic S1PR1 in competition-dependent astrocyte
507 tiling. To specifically test this, we deleted S1PR1 in two adjacent astrocytes in cortical areas by

508 coinjecting AAVs expressing YFP-P2A-Cre and tdTomato-P2A-Cre (KO:KO) or YFP and
509 tdTomato (WT:WT) under the control of the GfaABC$_1$D promoter into S1PR1$^{loxP/loxP}$ pups at P2-
510 3 (Fig. 8A-C). Although this strategy creates coinfection of YFP and tdTomato mostly within the
511 same astrocyte, in some instances an astrocyte is infected/labeled with only one (YFP or tdTomato)
512 fluorescent protein (Fig. 8B-D). Furthermore, in rare instances we found two adjacent astrocytes
513 labeled with YFP and tdTomato ideal for analyzing territorial overlap/tiling (we called these as
514 "Tiling pair" astrocytes) (Fig. 8D). After searching through several brain slices from 3 mice per
515 group we found and imaged ~18-23 tiling pair astrocytes. While we found minimal territorial
516 overlap amongst the WT:WT tiling pairs, astrocytes in the S1PR1 KO:KO tiling pair showed
517 extensive territorial overlap volume relative to their total volume captured (Fig. 8D,E). This data
518 clearly demonstrates that S1PR1 regulates astrocyte territorial volume overlap, causing a tiling
519 defect in a competition-dependent manner.

520 **Discussion**

521 Advancements in molecular profiling and super-resolution microscopy have identified
522 astrocytes as heterogenous cells that possess unique molecular, transcriptional, and morphological
523 characteristics[41,42]. Their tumultuous morphology enables them to engage in numerous
524 neurological functions through interactions with neurons, glia, and vasculature at both circuit and
525 synaptic levels. Thus, uncovering the mechanisms that establish these interactions is essential to
526 understanding the development and function of the mammalian brain. How astrocyte
527 morphogenesis and tiling are established in the mammalian brain is mostly unknown. Here we
528 demonstrate that the astrocyte-enriched G-protein coupled receptor S1PR1 influences
529 morphogenesis of murine astrocytes both *in vitro* and *in vivo*. Moreover, our data strongly suggest
530 that S1PR1 may play a role in establishing competition-driven astrocyte morphogenesis and tiling

531 and further propose that the bioactive lipid S1P drives astrocyte growth and tiling in a neuronal
532 contact-dependent manner.

533 **Neuronal contact induces S1PR1-dependent astrocyte morphogenesis *in vitro.***

534 In mouse astrocyte-neuron cocultures, we observed two distinct pools of astrocytes. One with high
535 S1PR1 and more complex morphology (astrocytes in contact with neurons) and the other with low
536 S1PR1 and less complex morphology (astrocytes without contact with neurons). This strongly
537 suggests that a contact-dependent signal, a labile soluble signal, or an extracellular matrix
538 component released or deposited locally by neurons may induce S1PR1 expression and astrocyte
539 morphogenesis. Indeed, our inhibitor data demonstrate that JAK-STAT3 but not SHH signaling
540 regulates S1PR1 expression and morphological complexity (Fig. 2). Although SHH is a soluble
541 signal released by deep-layer cortical neurons, it interacts with and activates PTCH1 in astrocytes
542 localized near the SHH expressing neuronal cell body[33]. Similarly, CT1 could also be locally
543 released by neurons to induce JAK-STAT3 signaling in astrocytes to regulate S1PR1 expression
544 and astrocyte morphogenesis. Because neurexin-neuroligin or delta-catenin-based cell adhesion
545 interactions between neuron and astrocyte have been shown to regulate astrocyte morphogenesis,
546 their involvement in S1PR1 expression cannot be ruled out here[30,43]. Interestingly, S1P-S1PR1 axis
547 has been shown to induce JAK-STAT3 signaling in cancer cells and that S1PR1 antagonist W146
548 inhibited expression of S1PR1 in cocultured astrocytes (Fig. 1K), it is possible that neuronal-
549 derived S1P could induce S1PR1 expression in cocultured astrocytes by enhancing JAK-STAT3
550 signaling. Because S1P can induce SHH expression through JAK–STAT3 activation in other cell
551 types[46], it is plausible that neuron-derived S1P similarly activates JAK–STAT3 in neurons to
552 promote SHH production, which then drives contact-dependent astrocyte morphogenesis. In
553 parallel, S1P directly signals through S1PR1–JAK–STAT3 in astrocytes to enhance their

554 morphological complexity. Thus, two distinct S1P-dependent pathways—one neuronal
555 (S1P→JAK–STAT3→SHH) and one astrocytic (S1P→S1PR1→JAK–STAT3)—may jointly
556 shape astrocyte development in our cocultures. This dual-pathway model also explains why
557 Ruxolitinib, which inhibits JAK–STAT3 in both neurons and astrocytes, produces a stronger
558 reduction in astrocyte complexity and S1PR1 expression than Sonidegib, which disrupts only the
559 SHH-dependent astrocyte complexity.

560 **S1PR1 regulates astrocyte morphogenesis in a cortical-layer dependent manner.**

561 AAV-mediated tracing of cytoplasm-filled or membrane-tagged GFP filled cortical astrocytes
562 revealed layer-specific differences in S1PR1-dependent astrocyte morphogenesis. We observed
563 that S1PR1 expression influenced the size, territory, and complexity of astrocytes in upper cortical
564 layers, whereas astrocytes in deeper layers appeared modestly affected. In agreement with our
565 findings, recent work has identified that cortical astrocytes are molecularly, structurally, and
566 functionally heterogeneous in a layer-specific manner[36,44]. Formation of the cortex occurs in a
567 well-described "inside-first, outside-last" pattern, where neural progenitor cells migrate to,
568 proliferate, and differentiate into neurons in deeper layers prior to upper layers[45,46]. Mouse
569 astrocytes begin to differentiate and interact with neurons toward the conclusion of embryogenesis
570 and the onset of corticogenesis; however, they do not achieve structural or functional maturation
571 until 3–4 weeks post-birth[5]. Notably, the expression of S1PR1 coincides with corticogenesis and
572 astrocyte maturation, gradually increasing during postnatal development and plateauing around
573 P30[28]. Given the temporal overlap between corticogenesis and S1PR1 expression, it is possible
574 that deeper layer astrocytes, which have formed connections with neurons, have already
575 structurally matured at P30 and no longer depend on S1PR1 activity. If true, deeper layer astrocytes
576 would exhibit morphological deficits at earlier developmental stages in the absence of S1PR1.

577 Alternatively, layer-specific differences in S1PR1-dependent astrocyte morphogenesis
578 may stem from inherent variations in basal S1PR1 expression across cortical layers. Spatial
579 transcriptomic analyses of the mouse cortex have revealed that S1PR1 is enriched in a
580 subpopulation of astrocytes localized within upper cortical layers[47]. Our immunofluorescent
581 staining shows that S1PR1 appears to have the strongest signal in upper cortical layers when
582 compared to deeper layers (Fig. 3C and data not shown). Consequently, higher expression of
583 S1PR1 in upper-layer astrocytes might correlate with increased S1PR1 activity. This suggests that
584 the S1P-S1PR1 signaling axis could be more pronounced within upper cortical layers, which could
585 explain our layer-specific differences.

586 Astrocyte morphogenesis is governed by a range of redundant molecular mechanisms that
587 vary by cortical layer. Cell-cell adhesion, neural activity, and neuron-secreted growth factors have
588 been described in regulating astrocyte morphogenesis and have been shown to be relevant in
589 different cortical layers[43,48,49]. For instance, loss of the signaling molecule Sonic hedgehog (Shh)
590 in layer-5 neurons reduced astrocyte complexity and tripartite synapse coverage; conversely, cell-
591 autonomous activation of Shh signaling in astrocytes promoted cortical excitatory synapse
592 formation[33]. Additionally, catenin-cadherin-mediated cell adhesion between neurons and
593 astrocytes in deeper cortical layers, not upper, established astrocyte morphological complexity[43].
594 Together, these findings underscore the existence of compensatory, layer-specific, and
595 bidirectional communication mechanisms that may mitigate the impact of S1PR1 loss in deeper
596 layer astrocytes.

597 **S1PR1 and Astrocyte Tiling**

598 Contrary to S1PR1$^{\Delta AST}$ astrocytes, deletion of S1PR1 from individual or sparse populations of
599 cortical astrocytes caused a reduction in astrocyte size, territory, and complexity, regardless of

600 cortical layer (Fig 6,7). Although consistent with our *in vitro* findings, these results contradict our
601 initial *in vivo* observations and raise the question: why does the ablation of S1PR1 in select
602 astrocytes result in a decrease in their overall size? A potential explanation could be competition.
603 Astrocytes occupy distinct, non-overlapping territories with neighboring astrocytes. Within a
604 single astrocyte territory, astrocytes have at least one main process that associates with blood
605 vessels and hundreds of finer processes that can contact thousands of synapses[50,51]. These domains
606 are formed by competitive, activity-dependent, and repulsive mechanisms that limit an astrocyte's
607 size, shape, and overall complexity[11,52]—a phenomenon referred to as tiling. Growth factor and
608 metabolite concentration gradients common in the brain[53] are used to drive chemotaxis of astrocyte
609 processes and neurites during postnatal brain development[54,55]. In the immune system,
610 maintenance of an S1P gradient between lymphatic tissue and the blood is important for the
611 extravasation of immune cells in an S1PR1-dependent manner[56]. Extracellular S1P levels are
612 regulated by the degradation of S1P into sphingosine via phospholipid phosphatases and
613 subsequent internalization[57,58]. Interestingly, activity of the lipid phosphatases Wunen (wun) and
614 Wunen2 (wun2) are implicated in S1PR1-dependent astrocytic tiling in zebrafish[29]. Furthermore,
615 it has been postulated that S1PR1 recycling is necessary for buffering extracellular S1P[59]. This
616 behavior is likely due to the docking of S1P's lipophilic sphingoid base into the binding cavity of
617 S1PR1 within the lipid membrane, followed by the subsequent endocytosis and degradation of
618 S1P-S1PR complexes[60]. This evidence indicates that lipid phosphatases and S1P receptors can
619 control levels of extracellular S1P and influence astrocyte process dynamics. Thus, in our sparse-
620 S1PR1 knockout model, a lack of S1PR1 could influence astrocyte morphogenesis by 1) regulating
621 cytoskeleton remodeling through S1PR1; and 2) indirectly promoting an excess of extracellular
622 S1P, which could favor adjacent wild-type astrocyte process outgrowth. However, the intercellular

623 mechanisms of S1P release, buffering, and degradation within the brain are still under
624 investigation.

625 **Potential Mechanisms of S1PR1 in Astrocyte Morphogenesis**

626 From lamellipodia formation to tumor cell metastasis, S1P-S1PR signaling has been implicated in
627 a diverse array of biomechanical processes[61–64]. In the mouse brain, S1PR1 primarily localizes to
628 fine astrocytic PAPs, which act as interfaces for astrocyte-neuron cross-communication[28]. The
629 remodeling of these PAPs in response to neuronal activity fine-tunes the regulation of
630 neurotransmitter clearance, ion exchange, and metabolite transport. S1PR1 has been directly
631 associated with modulation of Rac and Rho GTPase activity, molecular switches that regulate actin
632 filament dynamics necessary for astrocyte process motility[65,66]. Furthermore, deletion of S1PR1
633 or inactivation of sphingosine kinase 1 (SphK1)—one of the enzymes that converts sphingosine
634 into S1P—suppresses Rac1 activity and limits chemotaxis[67,68]. Therefore, the localization of
635 S1PR1 on PAPs positions the receptor as a potential regulator of PAP remodeling in response to
636 environmental and molecular cues such as neuronal activity[69]. Indeed, S1PR1 has been shown to
637 regulate Rac1-mediated actin remodeling of astrocyte processes in zebrafish, leading to dynamic
638 membrane extension and retraction[29], deficits in which generated smaller astrocytes. In support of
639 this, our results indicate that S1PR1 influences murine astrocyte size, territory, and complexity,
640 likely by regulation of process branching through actin remodeling. Moreover, S1PR1 KO
641 astrocytes mostly exhibited changes in finer, distal processes regardless of the KO model, as
642 evidenced by Sholl analyses (Figures 4-7 and S4). Thus, S1PR1 might be primed to regulate
643 dynamic, actin-dependent cytoskeletal remodeling in finer astrocytic processes.

644 **Consequences and Future Directions**

645 The formation and remodeling of fine astrocyte processes are essential for maintaining normal
646 astrocyte function, aberrations in which precede many neurological diseases[70–72]. Astrocytes
647 engage in dynamic interactions with both neurons and other glial cells to support the assembly,
648 maintenance, and functionality of neural circuits. Our findings highlight a critical role for S1PR1
649 in the structural maturation of astrocytes; however, the underlying intercellular mechanisms
650 driving this process remain poorly understood. Our in vitro experiments suggest that neuronal
651 contact induces astrocytic S1PR1 expression, while exogenous S1P stimulation enhances astrocyte
652 morphological complexity and upregulates synaptogenic factor expression[28]. These results raise
653 the possibility that neuron derived S1P may act in a paracrine manner on astrocytic S1PR1 to
654 promote tripartite synapse formation. Nonetheless, further investigation is needed to determine the
655 cellular source of S1P *in vivo* and to elucidate the functional consequences of disrupted S1PR1
656 signaling during normal brain development and disease.

657

658 ***Declarations***

659 ***Funding***

660 This work was supported by NIH grant R01NS126504 (to SKS). Microscopy was performed at
661 the VCU Microscopy Facility, supported, in part, with funding from the NIH-NCI Cancer Center
662 Support Grant P30 CA016059.

663 ***Competing interests***

664 The authors declare that they have no competing interests.

665 ***Authors` contributions***

666 C.T., J.P.G. and S.C.R.T. planned and performed most experiments, with assistance from Z.T.,
667 S.M., P.M., J.H., K.S. and O.D. SKS conceived the study and contributed to planning of the
668 experiments. C.T., J.P.G. and S.K.S. drafted the manuscript. All authors read and approved the
669 final manuscript.

670 ***Availability of data and material***

671 The data that support the findings of this study are available from the corresponding author upon
672 reasonable request.

673 ***Ethics approval***

674 Mice were housed at Virginia Commonwealth University according to guidelines of the
675 Institutional Animal Care Use Committee (IACUC). The mouse protocols were approved by the
676 IACUC. All mice were housed with food and water available ad libitum under a 12 h–12 h light–
677 dark cycle in a 20–22°C and 40–60% humidity environment.

678 ***Consent for publication***

679 Not applicable.

680

681

682

683

684

References

(1) Zuchero, J. B.; Barres, B. A. Glia in Mammalian Development and Disease. *Dev. Camb.* **2015**, *142* (22), 3805–3809. https://doi.org/10.1242/dev.129304.

(2) Xiong, H.; Tang, F.; Guo, Y.; Xu, R.; Lei, P. Neural Circuit Changes in Neurological Disorders: Evidence from in Vivo Two-Photon Imaging. *Ageing Res. Rev.* **2023**, *87*, 101933. https://doi.org/10.1016/j.arr.2023.101933.

(3) De Luca, C.; Colangelo, A. M.; Virtuoso, A.; Alberghina, L.; Papa, M. Neurons, Glia, Extracellular Matrix and Neurovascular Unit: A Systems Biology Approach to the Complexity of Synaptic Plasticity in Health and Disease. *Int. J. Mol. Sci.* **2020**, *21* (4), 1539. https://doi.org/10.3390/ijms21041539.

(4) Degl'Innocenti, E.; Dell'Anno, M. T. Human and Mouse Cortical Astrocytes: A Comparative View from Development to Morphological and Functional Characterization. *Front. Neuroanat.* **2023**, *17*. https://doi.org/10.3389/fnana.2023.1130729.

(5) Akdemir, E. S.; Huang, A. Y.-S.; Deneen, B. Astrocytogenesis: Where, When, and How. *F1000Research* **2020**, *9*, F1000 Faculty Rev-233. https://doi.org/10.12688/f1000research.22405.1.

(6) Chaboub, L. S.; Deneen, B. Developmental Origins of Astrocyte Heterogeneity: The Final Frontier of CNS Development. *Dev. Neurosci.* **2013**, *34* (5), 379–388. https://doi.org/10.1159/000343723.

(7) Bélanger, M.; Allaman, I.; Magistretti, P. J. Brain Energy Metabolism: Focus on Astrocyte-Neuron Metabolic Cooperation. *Cell Metab.* **2011**, *14* (6), 724–738. https://doi.org/10.1016/j.cmet.2011.08.016.

(8) Sun, M.; You, H.; Hu, X.; Luo, Y.; Zhang, Z.; Song, Y.; An, J.; Lu, H. Microglia–Astrocyte Interaction in Neural Development and Neural Pathogenesis. *Cells* **2023**, *12* (15), 1942. https://doi.org/10.3390/cells12151942.

(9) Lee, S. Y.; Chung, W.-S. The Roles of Astrocytic Phagocytosis in Maintaining Homeostasis of Brains. *J. Pharmacol. Sci.* **2021**, *145* (3), 223–227. https://doi.org/10.1016/j.jphs.2020.12.007.

(10) Molina-Gonzalez, I.; Holloway, R. K.; Jiwaji, Z.; Dando, O.; Kent, S. A.; Emelianova, K.; Lloyd, A. F.; Forbes, L. H.; Mahmood, A.; Skripuletz, T.; Gudi, V.; Febery, J. A.; Johnson, J. A.; Fowler, J. H.; Kuhlmann, T.; Williams, A.; Chandran, S.; Stangel, M.; Howden, A. J. M.; Hardingham, G. E.; Miron, V. E. Astrocyte-Oligodendrocyte Interaction Regulates Central Nervous System Regeneration. *Nat. Commun.* **2023**, *14* (1), 3372. https://doi.org/10.1038/s41467-023-39046-8.

719 (11) Baldwin, K. T.; Murai, K. K.; Khakh, B. S. Astrocyte Morphology. *Trends Cell Biol.* **2024**,
720 *34* (7), 547–565. https://doi.org/10.1016/j.tcb.2023.09.006.

721 (12) Lattke, M.; Guillemot, F. Understanding Astrocyte Differentiation: Clinical Relevance,
722 Technical Challenges, and New Opportunities in the Omics Era. *Wires Mech. Dis.* **2022**, *14*
723 (5), e1557. https://doi.org/10.1002/wsbm.1557.

724 (13) Sloan, S. A.; Barres, B. A. Mechanisms of Astrocyte Development and Their Contributions
725 to Neurodevelopmental Disorders. *Curr. Opin. Neurobiol.* **2014**, *27*, 75–81.
726 https://doi.org/10.1016/j.conb.2014.03.005.

727 (14) Stipursky, J.; Francis, D.; Dezonne, R. S.; Bérgamo de Araújo, A. P.; Souza, L.; Moraes, C.
728 A.; Alcantara Gomes, F. C. TGF-B1 Promotes Cerebral Cortex Radial Glia-Astrocyte
729 Differentiation in Vivo. *Front. Cell. Neurosci.* **2014**, *8*, 393.
730 https://doi.org/10.3389/fncel.2014.00393.

731 (15) Cahoy, J. D.; Emery, B.; Kaushal, A.; Foo, L. C.; Zamanian, J. L.; Christopherson, K. S.;
732 Xing, Y.; Lubischer, J. L.; Krieg, P. A.; Krupenko, S. A.; Thompson, W. J.; Barres, B. A. A
733 Transcriptome Database for Astrocytes, Neurons, and Oligodendrocytes: A New Resource
734 for Understanding Brain Development and Function. *J. Neurosci. Off. J. Soc. Neurosci.*
735 **2008**, *28* (1), 264–278. https://doi.org/10.1523/JNEUROSCI.4178-07.2008.

736 (16) van Meer, G.; Voelker, D. R.; Feigenson, G. W. Membrane Lipids: Where They Are and
737 How They Behave. *Nat. Rev. Mol. Cell Biol.* **2008**, *9* (2), 112–124.
738 https://doi.org/10.1038/nrm2330.

739 (17) Gault, C. R.; Obeid, L. M.; Hannun, Y. A. An Overview of Sphingolipid Metabolism: From
740 Synthesis to Breakdown. *Adv. Exp. Med. Biol.* **2010**, *688*, 1. https://doi.org/10.1007/978-1-
741 4419-6741-1_1.

742 (18) Simons, K.; Toomre, D. Lipid Rafts and Signal Transduction. *Nat. Rev. Mol. Cell Biol.*
743 **2000**, *1* (1), 31–39. https://doi.org/10.1038/35036052.

744 (19) Maceyka, M.; Spiegel, S. Sphingolipid Metabolites in Inflammatory Disease. *Nature* **2014**,
745 *510* (7503), 58–67. https://doi.org/10.1038/nature13475.

746 (20) Sonnino, S.; Prinetti, A. The Role of Sphingolipids in Neuronal Plasticity of the Brain. *J.*
747 *Neurochem.* **2016**, *137* (4), 485–488. https://doi.org/10.1111/jnc.13589.

748 (21) Yu, R. K.; Nakatani, Y.; Yanagisawa, M. The Role of Glycosphingolipid Metabolism in the
749 Developing Brain. *J. Lipid Res.* **2009**, *50* (SUPPL.), 440–445.
750 https://doi.org/10.1194/jlr.R800028-JLR200.

751 (22) Bassi, R.; Anelli, V.; Giussani, P.; Tettamanti, G.; Viani, P.; Riboni, L. Sphingosine-1-
752 Phosphate Is Released by Cerebellar Astrocytes in Response to bFGF and Induces

Astrocyte Proliferation through Gi-Protein-Coupled Receptors. *Glia* **2006**, *53* (6), 621–630. https://doi.org/10.1002/glia.20324.

(23) Sorensen, S. D.; Nicole, O.; Peavy, R. D.; Montoya, L. M.; Lee, C. J.; Murphy, T. J.; Traynelis, S. F.; Hepler, J. R. Common Signaling Pathways Link Activation of Murine PAR-1, LPA, and S1P Receptors to Proliferation of Astrocytes. *Mol. Pharmacol.* **2003**, *64* (5), 1199–1209. https://doi.org/10.1124/mol.64.5.1199.

(24) Young, N.; Van Brocklyn, J. R. Roles of Sphingosine-1-Phosphate (S1P) Receptors in Malignant Behavior of Glioma Cells. Differential Effects of S1P2 on Cell Migration and Invasiveness. *Exp. Cell Res.* **2007**, *313* (8), 1615–1627. https://doi.org/10.1016/j.yexcr.2007.02.009.

(25) Cencetti, F.; Bernacchioni, C.; Bruno, M.; Squecco, R.; Idrizaj, E.; Berbeglia, M.; Bruni, P.; Donati, C. Sphingosine 1-Phosphate-Mediated Activation of Ezrin-Radixin-Moesin Proteins Contributes to Cytoskeletal Remodeling and Changes of Membrane Properties in Epithelial Otic Vesicle Progenitors. *Biochim. Biophys. Acta BBA - Mol. Cell Res.* **2019**, *1866* (4), 554–565. https://doi.org/10.1016/j.bbamcr.2018.12.007.

(26) Paik, J. H.; Chae, S.; Lee, M.-J.; Thangada, S.; Hla, T. Sphingosine 1-Phosphate-Induced Endothelial Cell Migration Requires the Expression of EDG-1 and EDG-3 Receptors and Rho-Dependent Activation of Avβ3- and B1-Containing Integrins *. *J. Biol. Chem.* **2001**, *276* (15), 11830–11837. https://doi.org/10.1074/jbc.M009422200.

(27) Toman, R. E.; Payne, S. G.; Watterson, K. R.; Maceyka, M.; Lee, N. H.; Milstien, S.; Bigbee, J. W.; Spiegel, S. Differential Transactivation of Sphingosine-1-Phosphate Receptors Modulates NGF-Induced Neurite Extension. *J. Cell Biol.* **2004**, *166* (3), 381–392. https://doi.org/10.1083/jcb.200402016.

(28) Singh, S. K.; Kordula, T.; Spiegel, S. Neuronal Contact Upregulates Astrocytic Sphingosine-1-Phosphate Receptor 1 to Coordinate Astrocyte-Neuron Cross Communication. *Glia* **2022**, *70* (4), 712–727. https://doi.org/10.1002/glia.24135.

(29) Chen, J.; Stork, T.; Kang, Y.; Nardone, K. A. M.; Auer, F.; Farrell, R. J.; Jay, T. R.; Heo, D.; Sheehan, A.; Paton, C.; Nagel, K. I.; Schoppik, D.; Monk, K. R.; Freeman, M. R. Astrocyte Growth Is Driven by the Tre1/S1pr1 Phospholipid-Binding G Protein-Coupled Receptor. *Neuron* **2024**, *112* (1), 93-112.e10. https://doi.org/10.1016/j.neuron.2023.11.008.

(30) Singh, S. K.; Stogsdill, J. A.; Pulimood, N. S.; Dingsdale, H.; Kim, Y. H.; Pilaz, L.-J.; Kim, I. H.; Manhaes, A. C.; Rodrigues, W. S.; Pamukcu, A.; Enustun, E.; Ertuz, Z.; Scheiffele, P.; Soderling, S. H.; Silver, D. L.; Ji, R.-R.; Medina, A. E.; Eroglu, C. Astrocytes Assemble Thalamocortical Synapses by Bridging NRX1α and NL1 via Hevin. *Cell* **2016**, *164* (1), 183–196. https://doi.org/10.1016/j.cell.2015.11.034.

788 (31) Uezu, A.; Kanak, D. J.; Bradshaw, T. W. A.; Soderblom, E. J.; Catavero, C. M.; Burette, A.
789 C.; Weinberg, R. J.; Soderling, S. H. Identification of an Elaborate Complex Mediating
790 Postsynaptic Inhibition. *Science* **2016**, *353* (6304), 1123–1129.
791 https://doi.org/10.1126/science.aag0821.

792 (32) Liddelow, S. A. Modern Approaches to Investigating Non-Neuronal Aspects of
793 Alzheimer's Disease. *FASEB J. Off. Publ. Fed. Am. Soc. Exp. Biol.* **2019**, *33* (2), 1528–
794 1535. https://doi.org/10.1096/fj.201802592.

795 (33) Gonzalez-Cabrera, P. J.; Jo, E.; Sanna, M. G.; Brown, S.; Leaf, N.; Marsolais, D.;
796 Schaeffer, M.-T.; Chapman, J.; Cameron, M.; Guerrero, M.; Roberts, E.; Rosen, H. Full
797 Pharmacological Efficacy of a Novel S1P1 Agonist That Does Not Require S1P-like
798 Headgroup Interactions. *Mol. Pharmacol.* **2008**, *74* (5), 1308–1318.
799 https://doi.org/10.1124/mol.108.049783.

800 (34) Acaz-Fonseca, E.; Ortiz-Rodriguez, A.; Azcoitia, I.; Garcia-Segura, L. M.; Arevalo, M.-A.
801 Notch Signaling in Astrocytes Mediates Their Morphological Response to an Inflammatory
802 Challenge. *Cell Death Discov.* **2019**, *5* (1), 85. https://doi.org/10.1038/s41420-019-0166-6.

803 (35) Xie, Y.; Kuan, A. T.; Wang, W.; Herbert, Z. T.; Mosto, O.; Olukoya, O.; Adam, M.; Vu, S.;
804 Kim, M.; Tran, D.; Gómez, N.; Charpentier, C.; Sorour, I.; Lacey, T. E.; Tolstorukov, M.
805 Y.; Sabatini, B. L.; Lee, W.-C. A.; Harwell, C. C. Astrocyte-Neuron Crosstalk through
806 Hedgehog Signaling Mediates Cortical Synapse Development. *Cell Rep.* **2022**, *38* (8),
807 110416. https://doi.org/10.1016/j.celrep.2022.110416.

808 (36) Hong, S.; Song, M.-R. STAT3 but Not STAT1 Is Required for Astrocyte Differentiation.
809 *PLOS ONE* **2014**, *9* (1), e86851. https://doi.org/10.1371/journal.pone.0086851.

810 (37) Yanagida, K.; Liu, C. H.; Faraco, G.; Galvani, S.; Smith, H. K.; Burg, N.; Anrather, J.;
811 Sanchez, T.; Iadecola, C.; Hla, T. Size-Selective Opening of the Blood–Brain Barrier by
812 Targeting Endothelial Sphingosine 1–Phosphate Receptor 1. *Proc. Natl. Acad. Sci.* **2017**,
813 *114* (17), 4531–4536. https://doi.org/10.1073/pnas.1618659114.

814 (38) Baldwin, K. T.; Tan, C. X.; Strader, S. T.; Jiang, C.; Savage, J. T.; Elorza-Vidal, X.;
815 Contreras, X.; Rülicke, T.; Hippenmeyer, S.; Estévez, R.; Ji, R. R.; Eroglu, C. HepaCAM
816 Controls Astrocyte Self-Organization and Coupling. *Neuron* **2021**, *109* (15), 2427-
817 2442.e10. https://doi.org/10.1016/j.neuron.2021.05.025.

818 (39) Lanjakornsiripan, D.; Pior, B. J.; Kawaguchi, D.; Furutachi, S.; Tahara, T.; Katsuyama, Y.;
819 Suzuki, Y.; Fukazawa, Y.; Gotoh, Y. Layer-Specific Morphological and Molecular
820 Differences in Neocortical Astrocytes and Their Dependence on Neuronal Layers. *Nat.*
821 *Commun.* **2018**, *9* (1). https://doi.org/10.1038/s41467-018-03940-3.

822 (40) Singh, S. K.; Weigel, C.; Brown, R. D. R.; Green, C. D.; Tuck, C.; Salvemini, D.; Spiegel,
823 S. FTY720/Fingolimod Mitigates Paclitaxel-Induced Sparcl1-Driven Neuropathic Pain and

824 Breast Cancer Progression. *FASEB J. Off. Publ. Fed. Am. Soc. Exp. Biol.* **2024**, *38* (15),
825 e23872. https://doi.org/10.1096/fj.202401277R.

826 (41) Chen, Z.; Doyle, T. M.; Luongo, L.; Largent-Milnes, T. M.; Giancotti, L. A.; Kolar, G.;
827 Squillace, S.; Boccella, S.; Walker, J. K.; Pendleton, A.; Spiegel, S.; Neumann, W. L.;
828 Vanderah, T. W.; Salvemini, D. Sphingosine-1-Phosphate Receptor 1 Activation in
829 Astrocytes Contributes to Neuropathic Pain. *Proc. Natl. Acad. Sci. U. S. A.* **2019**, *116* (21),
830 10557–10562. https://doi.org/10.1073/pnas.1820466116.

831 (42) Kim, S. K.; Hayashi, H.; Ishikawa, T.; Shibata, K.; Shigetomi, E.; Shinozaki, Y.; Inada, H.;
832 Roh, S. E.; Kim, S. J.; Lee, G.; Bae, H.; Moorhouse, A. J.; Mikoshiba, K.; Fukazawa, Y.;
833 Koizumi, S.; Nabekura, J. Cortical Astrocytes Rewire Somatosensory Cortical Circuits for
834 Peripheral Neuropathic Pain. *J. Clin. Invest.* **2016**, *126* (5), 1983–1997.
835 https://doi.org/10.1172/JCI82859.

836 (43) Reeves, A. M. B.; Shigetomi, E.; Khakh, B. S. Bulk Loading of Calcium Indicator Dyes to
837 Study Astrocyte Physiology: Key Limitations and Improvements Using Morphological
838 Maps. *J. Neurosci.* **2011**, *31* (25), 9353–9358. https://doi.org/10.1523/JNEUROSCI.0127-
839 11.2011.

840 (44) Batiuk, M. Y.; Martirosyan, A.; Wahis, J.; de Vin, F.; Marneffe, C.; Kusserow, C.;
841 Koeppen, J.; Viana, J. F.; Oliveira, J. F.; Voet, T.; Ponting, C. P.; Belgard, T. G.; Holt, M.
842 G. Identification of Region-Specific Astrocyte Subtypes at Single Cell Resolution. *Nat.*
843 *Commun.* **2020**, *11* (1), 1220. https://doi.org/10.1038/s41467-019-14198-8.

844 (45) Peng, H.; Xie, P.; Liu, L.; Kuang, X.; Wang, Y.; Qu, L.; Gong, H.; Jiang, S.; Li, A.; Ruan,
845 Z.; Ding, L.; Yao, Z.; Chen, C.; Chen, M.; Daigle, T. L.; Dalley, R.; Ding, Z.; Duan, Y.;
846 Feiner, A.; He, P.; Hill, C.; Hirokawa, K. E.; Hong, G.; Huang, L.; Kebede, S.; Kuo, H. C.;
847 Larsen, R.; Lesnar, P.; Li, L.; Li, Q.; Li, X.; Li, Y.; Li, Y.; Liu, A.; Lu, D.; Mok, S.; Ng, L.;
848 Nguyen, T. N.; Ouyang, Q.; Pan, J.; Shen, E.; Song, Y.; Sunkin, S. M.; Tasic, B.; Veldman,
849 M. B.; Wakeman, W.; Wan, W.; Wang, P.; Wang, Q.; Wang, T.; Wang, Y.; Xiong, F.;
850 Xiong, W.; Xu, W.; Ye, M.; Yin, L.; Yu, Y.; Yuan, J.; Yuan, J.; Yun, Z.; Zeng, S.; Zhang,
851 S.; Zhao, S.; Zhao, Z.; Zhou, Z.; Huang, Z. J.; Esposito, L.; Hawrylycz, M. J.; Sorensen, S.
852 A.; Yang, X. W.; Zheng, Y.; Gu, Z.; Xie, W.; Koch, C.; Luo, Q.; Harris, J. A.; Wang, Y.;
853 Zeng, H. Morphological Diversity of Single Neurons in Molecularly Defined Cell Types.
854 *Nature* **2021**, *598* (7879), 174–181. https://doi.org/10.1038/s41586-021-03941-1.

855 (46) Tan, C. X.; Bindu, D. S.; Hardin, E. J.; Sakers, K.; Baumert, R.; Ramirez, J. J.; Savage, J.
856 T.; Eroglu, C. δ-Catenin Controls Astrocyte Morphogenesis via Layer-Specific Astrocyte–
857 Neuron Cadherin Interactions. *J. Cell Biol.* **2023**, *222* (11), e202303138.
858 https://doi.org/10.1083/jcb.202303138.

859 (47) Yan, X.; Li, S.; Wang, J.; Wang, Q.; Xie, X.; Li, M. Sphingosine-1-Phosphate Induces
860 Pulmonary Artery Smooth Muscle Cell Proliferation, Migration and Pulmonary Arterial

Remodeling by Modulating Sonic Hedgehog Signaling Effector FoxM1. *Chin. Med. J. (Engl.)* **2026**. https://doi.org/10.1097/CM9.0000000000004041.

(48) Bayraktar, O. A.; Bartels, T.; Holmqvist, S.; Kleshchevnikov, V.; Martirosyan, A.; Polioudakis, D.; Ben Haim, L.; Young, A. M. H.; Batiuk, M. Y.; Prakash, K.; Brown, A.; Roberts, K.; Paredes, M. F.; Kawaguchi, R.; Stockley, J. H.; Sabeur, K.; Chang, S. M.; Huang, E.; Hutchinson, P.; Ullian, E. M.; Hemberg, M.; Coppola, G.; Holt, M. G.; Geschwind, D. H.; Rowitch, D. H. Astrocyte Layers in the Mammalian Cerebral Cortex Revealed by a Single-Cell in Situ Transcriptomic Map. *Nat. Neurosci.* **2020**, *23* (4), 500–509. https://doi.org/10.1038/s41593-020-0602-1.

(49) Lee, J. Y. Normal and Disordered Formation of the Cerebral Cortex : Normal Embryology, Related Molecules, Types of Migration, Migration Disorders. *J. Korean Neurosurg. Soc.* **2019**, *62* (3), 265–271. https://doi.org/10.3340/jkns.2019.0098.

(50) Wu, M. W.; Kourdougli, N.; Portera-Cailliau, C. Network State Transitions during Cortical Development. *Nat. Rev. Neurosci.* **2024**, *25* (8), 535–552. https://doi.org/10.1038/s41583-024-00824-y.

(51) Bocchi, R.; Thorwirth, M.; Simon-Ebert, T.; Koupourtidou, C.; Clavreul, S.; Kolf, K.; Della Vecchia, P.; Bottes, S.; Jessberger, S.; Zhou, J.; Wani, G.; Pilz, G.-A.; Ninkovic, J.; Buffo, A.; Sirko, S.; Götz, M.; Fischer-Sternjak, J. Astrocyte Heterogeneity Reveals Region-Specific Astrogenesis in the White Matter. *Nat. Neurosci.* **2025**, *28* (3), 457–469. https://doi.org/10.1038/s41593-025-01878-6.

(52) Cheng, Y.-T.; Luna-Figueroa, E.; Woo, J.; Chen, H.-C.; Lee, Z.-F.; Harmanci, A. S.; Deneen, B. Inhibitory Input Directs Astrocyte Morphogenesis through Glial GABABR. *Nature* **2023**, *617* (7960), 369–376. https://doi.org/10.1038/s41586-023-06010-x.

(53) Holt, L. M.; Hernandez, R. D.; Pacheco, N. L.; Torres Ceja, B.; Hossain, M.; Olsen, M. L. Astrocyte Morphogenesis Is Dependent on BDNF Signaling via Astrocytic TrkB.T1. *eLife* **2019**, *8*, 1–27. https://doi.org/10.7554/eLife.44667.

(54) Bushong, E. A.; Martone, M. E.; Jones, Y. Z.; Ellisman, M. H. Protoplasmic Astrocytes in CA1 Stratum Radiatum Occupy Separate Anatomical Domains. *J. Neurosci.* **2002**, *22* (1), 183–192. https://doi.org/10.1523/jneurosci.22-01-00183.2002.

(55) Shigetomi, E.; Bushong, E. A.; Haustein, M. D.; Tong, X.; Jackson-Weaver, O.; Kracun, S.; Xu, J.; Sofroniew, M. V.; Ellisman, M. H.; Khakh, B. S. Imaging Calcium Microdomains within Entire Astrocyte Territories and Endfeet with GCaMPs Expressed Using Adeno-Associated Viruses. *J. Gen. Physiol.* **2013**, *141* (5), 633–647. https://doi.org/10.1085/jgp.201210949.

(56) Hayashi, M. K.; Sato, K.; Sekino, Y. Neurons Induce Tiled Astrocytes with Branches That Avoid Each Other. *Int. J. Mol. Sci.* **2022**, *23* (8). https://doi.org/10.3390/ijms23084161.

(57) Sansom, S. N.; Livesey, F. J. Gradients in the Brain: The Control of the Development of Form and Function in the Cerebral Cortex. *Cold Spring Harb. Perspect. Biol.* **2009**, *1* (2), a002519. https://doi.org/10.1101/cshperspect.a002519.

(58) Neal, M.; Luo, D.; Harischandra, D. S.; Gordon, R.; Sarkar, S.; Jin, H.; Anantharam, V.; Désaubry, L.; Kanthasamy, A.; Kanthasamy, A. Prokineticin-2 Promotes Chemotaxis and Alternative A2 Reactivity of Astrocytes. *Glia* **2018**, *66* (10), 2137–2157. https://doi.org/10.1002/glia.23467.

(59) Bicknell, B. A.; Pujic, Z.; Feldner, J.; Vetter, I.; Goodhill, G. J. Chemotactic Responses of Growing Neurites to Precisely Controlled Gradients of Nerve Growth Factor. *Sci. Data* **2018**, *5* (1), 180183. https://doi.org/10.1038/sdata.2018.183.

(60) Rivera, J.; Proia, R. L.; Olivera, A. THE ALLIANCE OF SPHINGOSINE-1-PHOSPHATE AND ITS RECEPTORS IN IMMUNITY. *Nat. Rev. Immunol.* **2008**, *8* (10), 753–763. https://doi.org/10.1038/nri2400.

(61) Kharel, Y.; Huang, T.; Salamon, A.; Harris, T. E.; Santos, W. L.; Lynch, K. R. Mechanism of Sphingosine 1-Phosphate Clearance from Blood. *Biochem. J.* **2020**, *477* (5), 925–935. https://doi.org/10.1042/BCJ20190730.

(62) Kono, M.; Mi, Y.; Liu, Y.; Sasaki, T.; Allende, M. L.; Wu, Y.-P.; Yamashita, T.; Proia, R. L. The Sphingosine-1-Phosphate Receptors S1P1, S1P2, and S1P3 Function Coordinately during Embryonic Angiogenesis*. *J. Biol. Chem.* **2004**, *279* (28), 29367–29373. https://doi.org/10.1074/jbc.M403937200.

(63) Gatfield, J.; Monnier, L.; Studer, R.; Bolli, M. H.; Steiner, B.; Nayler, O. Sphingosine-1-Phosphate (S1P) Displays Sustained S1P1 Receptor Agonism and Signaling through S1P Lyase-Dependent Receptor Recycling. *Cell. Signal.* **2014**, *26* (7), 1576–1588. https://doi.org/10.1016/j.cellsig.2014.03.029.

(64) Yuan, Y.; Jia, G.; Wu, C.; Wang, W.; Cheng, L.; Li, Q.; Li, Z.; Luo, K.; Yang, S.; Yan, W.; Su, Z.; Shao, Z. Structures of Signaling Complexes of Lipid Receptors S1PR1 and S1PR5 Reveal Mechanisms of Activation and Drug Recognition. *Cell Res.* **2021**, *31* (12), 1263–1274. https://doi.org/10.1038/s41422-021-00566-x.

(65) Donati, C.; Bruni, P. Sphingosine 1-Phosphate Regulates Cytoskeleton Dynamics: Implications in Its Biological Response. *Biochim. Biophys. Acta BBA - Biomembr.* **2006**, *1758* (12), 2037–2048. https://doi.org/10.1016/j.bbamem.2006.06.015.

(66) Ko, P.; Kim, D.; You, E.; Jung, J.; Oh, S.; Kim, J.; Lee, K.-H.; Rhee, S. Extracellular Matrix Rigidity-Dependent Sphingosine-1-Phosphate Secretion Regulates Metastatic Cancer Cell Invasion and Adhesion. *Sci. Rep.* **2016**, *6* (1), 21564. https://doi.org/10.1038/srep21564.

(67) Lee, J.-F.; Ozaki, H.; Zhan, X.; Wang, E.; Hla, T.; Lee, M.-J. Sphingosine-1-Phosphate Signaling Regulates Lamellipodia Localization of Cortactin Complexes in Endothelial Cells. *Histochem. Cell Biol.* **2006**, *126* (3), 297–304. https://doi.org/10.1007/s00418-006-0143-z.

(68) Sassoli, C.; Pierucci, F.; Zecchi-Orlandini, S.; Meacci, E. Sphingosine 1-Phosphate (S1P)/ S1P Receptor Signaling and Mechanotransduction: Implications for Intrinsic Tissue Repair/Regeneration. *Int. J. Mol. Sci.* **2019**, *20* (22), 5545. https://doi.org/10.3390/ijms20225545.

(69) Haber, M.; Zhou, L.; Murai, K. K. Cooperative Astrocyte and Dendritic Spine Dynamics at Hippocampal Excitatory Synapses. *J. Neurosci. Off. J. Soc. Neurosci.* **2006**, *26* (35), 8881–8891. https://doi.org/10.1523/JNEUROSCI.1302-06.2006.

(70) Murk, K.; Blanco Suarez, E. M.; Cockbill, L. M. R.; Banks, P.; Hanley, J. G. The Antagonistic Modulation of Arp2/3 Activity by N-WASP, WAVE2 and PICK1 Defines Dynamic Changes in Astrocyte Morphology. *J. Cell Sci.* **2013**, *126* (Pt 17), 3873–3883. https://doi.org/10.1242/jcs.125146.

(71) Hobson, J. P.; Rosenfeldt, H. M.; Barak, L. S.; Olivera, A.; Poulton, S.; Caron, M. G.; Milstien, S.; Spiegel, S. Role of the Sphingosine-1-Phosphate Receptor EDG-1 in PDGF-Induced Cell Motility. *Science* **2001**, *291* (5509), 1800–1803. https://doi.org/10.1126/science.1057559.

(72) Lee, M.-J.; Thangada, S.; Paik, J.-H.; Sapkota, G. P.; Ancellin, N.; Chae, S.-S.; Wu, M.; Morales-Ruiz, M.; Sessa, W. C.; Alessi, D. R.; Hla, T. Akt-Mediated Phosphorylation of the G Protein-Coupled Receptor EDG-1 Is Required for Endothelial Cell Chemotaxis. *Mol. Cell* **2001**, *8* (3), 693–704. https://doi.org/10.1016/S1097-2765(01)00324-0.

(73) Schiweck, J.; Eickholt, B. J.; Murk, K. Important Shapeshifter: Mechanisms Allowing Astrocytes to Respond to the Changing Nervous System during Development, Injury and Disease. *Front. Cell. Neurosci.* **2018**, *12* (August), 1–17. https://doi.org/10.3389/fncel.2018.00261.

(74) Schober, A. L.; Wicki-Stordeur, L. E.; Murai, K. K.; Swayne, L. A. Foundations and Implications of Astrocyte Heterogeneity during Brain Development and Disease. *Trends Neurosci.* **2022**, *45* (9), 692–703. https://doi.org/10.1016/j.tins.2022.06.009.

(75) Badia-Soteras, A.; Mak, A.; Blok, T. M.; Boers-Escuder, C.; van den Oever, M. C.; Min, R.; Smit, A. B.; Verheijen, M. H. G. Astrocyte-Synapse Structural Plasticity in Neurodegenerative and Neuropsychiatric Diseases. *Biol. Psychiatry* **2025**. https://doi.org/10.1016/j.biopsych.2025.04.011.

(76) Endo, F.; Kasai, A.; Soto, J. S.; Yu, X.; Qu, Z.; Hashimoto, H.; Gradinaru, V.; Kawaguchi, R.; Khakh, B. S. Molecular Basis of Astrocyte Diversity and Morphology across the CNS

in Health and Disease. *Science* **2022**, *378* (6619), eadc9020. https://doi.org/10.1126/science.adc9020.

987 **Figure legends**

988 **Fig 1. Astrocyte morphology and S1PR1 expression is driven by neuronal contact *in vitro*.**
989 Representative confocal images (20X) of S1PR1-GFP astrocytes (green) cultured alone (**A only**)
990 or with WT neurons (**A+N**) stained with Map2 (red) for 8 **(A-D)** or 24 hours (**E-H**). Based on the
991 astrocytes interaction with or without Map2+ neuronal processes in A+N cocultures, astrocytes
992 were separated into either non-interacting astrocytes (NIA) (Blue arrow in E) or interacting
993 astrocytes (IA) (white arrow in E). Quantification of perimeter (**B** and **F**) and S1PR1 expression
994 as green signal intensity (**C** and **G**) per astrocyte, respectively, in A or A+N cultures. (**D** and **H**)
995 Quantification of astrocyte morphological complexity as indicated by number of intersections
996 plotted against distance from center of the soma by Sholl analyses from A or A+N cultures. (**I-L**)
997 S1PR1 inhibition blocks neuronal contact dependent astrocyte morphological complexity. (**I**)
998 Representative confocal image of S1PR1-GFP astrocytes treated with vehicle (DMSO) or the
999 S1PR1 antagonist, W146, for 24 hours cultured with or without neurons (Map2, red). Perimeter
1000 (**J**) and fluorescent intensity (**K**) analyses of GFP immunofluorescence from S1PR1-GFP
1001 astrocytes. (**L**) Quantification of morphological complexity of astrocytes as indicated by number
1002 of intersections plotted against distance from center of the soma by Sholl analyses. Data represents
1003 the mean ± SEM from two- (A-H) or three (I-L) -biological replicates. * = $p<0.05$, *** = $p < 0.001$,
1004 **** = $p<0.0001$; one way ANOVA.

1005

1006 **Fig 2. JAK/STAT but not Sonic hedgehog signaling regulates neuronal contact-induced**
1007 **S1PR1 expression in astrocytes. (A)** Representative confocal images (20X) of S1PR1-GFP
1008 astrocytes (green) cultured alone (**A only**) or with WT neurons (**A+N**) stained with Map2 (red)
1009 treated with vehicle (DMSO), the JAK2 inhibitor Ruxolitinib (Rux), or the Smoothened inhibitor

1010 Sonidegib (Sonid), for 24 hours. Quantification of perimeter (**B**) and level of S1PR1 expression as
1011 fluorescent signal intensity (**C**) per astrocyte respectively in A or A+N cultures. (**D, E**)
1012 Quantification of astrocyte morphological complexity as indicated by the number of intersections
1013 plotted against distance from center of the soma by Sholl analyses from A or A+N cultures treated
1014 with vehicle (DMSO) control, Rux, or Sonid. Data represents the mean ± SEM from three
1015 biological replicates. ** = $p<0.01$, *** = $p < 0.001$, **** = $p<0.0001$, one way ANOVA.

1016

1017 **Fig 3. Astrocyte-specific, S1PR1 knock-out mice (S1PR1$^{\Delta As t}$) exhibit no gross changes in**
1018 **blood vasculature and astrocyte maturation.** (**A**) Astrocyte-specific, S1PR1 knock-out mouse
1019 model (S1PR1$^{\Delta AST}$) model. (**B**) A substantial reduction in S1PR1 mRNA levels measured by
1020 qPCR. ((n=8 and 7 mice per group). **(C)** Representative confocal images of S1PR1 (green) with
1021 the endothelial marker CD31 (red) from S1PR1$^{\Delta AST}$ or littermate control cortices at P30. Arrows
1022 indicate intact S1PR1 expression on CD31+ vasculature. (**D**) Quantification of CD31 intensity
1023 represented as area per image is not altered in S1PR1$^{\Delta AST}$ cortices at P30. (**F**) Blood-brain barrier
1024 integrity assay scheme (left) and quantification of tracer dyes 1 kDa Cadaverine (center) and 3
1025 kDa Dextran (right) signal in S1PR1$^{\Delta AST}$ cortices at ~P35 indicates intact BBB integrity in
1026 S1PR1$^{\Delta AST}$ mice. (**G**) Representative image (top) and quantifications of GFAP signal (green) in
1027 S1PR1$^{\Delta AST}$ cortices at P30. (**H**) Representative image of perisynaptic astrocyte marker GLT-1 (red)
1028 with S1PR1 (green) in S1PR1$^{\Delta AST}$ cortices at P30 (top). Quantification of GLT1 puncta measured
1029 as GLT1-spot count and -spot volume by IMARIS 3D rendering indicate no changes in GLT1
1030 expression in S1PR1$^{\Delta AST}$ cortices at P30. Data represents the mean ± SEM from n=3 and 4 mice
1031 per group (D-H). *** = $p < 0.001$, ns=not significant; Unpaired Two-tailed student`s T-test.

1032

1033 **Fig 4. L2-3 S1PR1$^{\Delta AST}$ astrocytes exhibit increased morphology and complexity.** (**A**)
1034 S1PR1$^{\Delta AST}$ or littermate controls were intracranially injected with the adenoassociated virus
1035 (AAV), pZac2.1-GfaABC1D-YFP, to sparsely label astrocytes. Sparsely labeled astrocytes from
1036 L2-3 somatosensory cortices were imaged and analyzed. (**B**) Representative confocal images and
1037 subsequent IMARIS 3D surface/filament renderings of YFP astrocytes from S1PR1$^{\Delta AST}$ or
1038 littermate controls at P30. **(C)** Quantification of astrocyte volume (left), and soma volume (right)
1039 from surface renderings generated using IMARIS. (**D**) Quantification of astrocyte territory volume
1040 (left), astrocyte process/filament length (middle) and area (right) from filament traces generated
1041 using IMARIS. (**E**) Plot depicting the proportion of astrocyte filament thicknesses grouped by
1042 mean diameter and represented as % of total filaments. (**F**) Sholl analyses of IMARIS rendered
1043 filament traces of astrocytes from S1PR1$^{\Delta AST}$ and littermate controls. Data represents the mean ±
1044 SEM from total 26 and 25 astrocytes from n=5 mice per group. * = $p<0.05$, *** = $p<0.001$, ns=non-
1045 significant, Unpaired Welch`s T-test.

1046

1047 **Fig 5. L4-5 S1PR1$^{\Delta AST}$ astrocytes exhibit a milder perturbation in astrocyte morphology.** (**A**)
1048 Sparsely YFP-labeled L4-5 somatosensory cortical astrocytes were imaged and analyzed. **(B)**
1049 Representative confocal images and subsequent IMARIS 3D surface/filament renderings of YFP
1050 astrocytes from S1PR1$^{\Delta AST}$ or littermate controls at P30. **(C)** Quantification of astrocyte volume
1051 (left) and soma volume (right) from surface renderings generated using IMARIS. (**D**)
1052 Quantification of astrocyte territory volume (left), astrocyte process/filament length (middle) and
1053 area (right) from filament traces generated using IMARIS. (**E**) Plot depicting the proportion of
1054 astrocyte filaments grouped at various mean diameter and represented as % of total filaments
1055 revealed no differences in mean dendrites in S1PR1$^{\Delta AST}$ astrocytes. (**F**) Sholl analyses of IMARIS

1056 rendered filament traces of astrocytes from S1PR1$^{\Delta AST}$ and littermate controls. Data represents the
1057 mean ± SEM of 24 and 22 astrocytes from n=5 mice per group. * = p<0.05, ** = p<0.01, ns=non-
1058 significant, Unpaired Welch`s T-test.

1059

1060 **Fig 6. Sparse deletion of S1PR1 in L2-3 astrocytes results in reduced astrocyte size and**
1061 **morphological complexity. (A)** Schematics showing S1PR1 deletion in sparse astrocytes by
1062 delivering AAV-GfaABC1D-YFP-P2A-Cre or AAV-GfaABC1D-YFP control in S1PR1$^{fl/fl}$ mouse
1063 pups. **(B)** Sparsely labeled astrocytes were imaged from L2-3 somatosensory cortex from P30
1064 pups. (**C**) Representative confocal images and subsequent IMARIS 3D surface/filament renderings
1065 of YFP astrocytes from S1PR1$^{\Delta AST}$ or littermate controls at P30. **(D)** Quantification of astrocyte
1066 volume (left) and soma volume (right) from Surface renderings generated by IMARIS. (**E**)
1067 Quantification of astrocyte territory volume (left) filament length (middle) and filament area
1068 (right) from filament traces generated by IMARIS. **(F)** Plot depicting the proportion of astrocyte
1069 filaments grouped by various mean diameter and represented as % of total filaments revealed no
1070 differences in mean dendrites in S1PR1$^{\Delta AST}$ astrocytes. (**G**) Sholl analyses of IMARIS rendered
1071 filament traces of YFP labeled sparse astrocytes from S1PR1$^{\Delta AST}$ and littermate controls. Data
1072 represents the mean ± SEM of 23 and 24 astrocytes from n=4 mice per group. * = p<0.05, ** =
1073 p<0.01, ns=non-significant, Unpaired Welch`s T-test.

1074

1075 **Fig 7. Sparse deletion of S1PR1 in L4-5 astrocytes results in reduced astrocyte size and**
1076 **morphological complexity. (A)** Schematics showing S1PR1 deletion in sparse astrocytes by
1077 delivering AAV-GfaABC1D-YFP-P2A-Cre or AAV-GfaABC1D-YFP control in S1PR1$^{fl/fl}$ mouse

1078 pups. Sparsely labeled astrocytes were imaged from L4-5 somatosensory cortex from P30 pups.
1079 (**B**) Representative confocal images and subsequent IMARIS 3D surface/filament renderings of
1080 YFP astrocytes from S1PR1$^{\Delta AST}$ or littermate controls at P30. **(C)** Quantification of astrocyte
1081 volume (left) and soma volume (right) from Surface renderings generated by IMARIS. (**E**)
1082 Quantification of astrocyte territory volume (left) process/filament length (middle) and area (left)
1083 from filament traces generated by IMARIS. **(F)** Plot depicting the proportion of astrocyte filaments
1084 grouped by mean diameter and represented as % of total filaments revealed no differences in mean
1085 dendrites in S1PR1$^{\Delta AST}$ astrocytes. (**G**) Sholl analyses of IMARIS rendered filament traces of GFP
1086 labeled sparse astrocytes from S1PR1$^{\Delta AST}$ and littermate controls. Data represents the mean ± SEM
1087 of 22 and 17 astrocytes from n=4 mice per group. * = $p<0.05$, ** = $p<0.01$, *** = $p<0.001$ ns=non-
1088 significant, Unpaired Welch`s T-test.

1089

1090 **Fig 8. Neighboring S1PR1 KO astrocytes exhibit increased astrocyte territory overlap. (A,**
1091 **B)** Schematics showing S1PR1 deletion in neighboring astrocytes in two-color schemes by
1092 delivering AAV-GfaABC1D-YFP-P2A-Cre plus AAV-GfaABC1D-tdTomato-P2A-Cre or AAV-
1093 GfaABC1D-YFP plus AAV-GfaABC1D-tdTomato controls in S1PR1$^{fl/fl}$ mouse pups. (**C**) Example
1094 20x confocal image to show the labelling by two color viruses. **(D)** Representative confocal images
1095 and subsequent IMARIS 3D surface/filament renderings to create territories of neighboring
1096 astrocytes from KO:KO or littermate WT:WT controls at P30. **(E)** Quantification of astrocyte
1097 territory overlap volume represented as % of total volume from two neighboring astrocytes. Data
1098 represents the mean ± SEM of 23 and 18 pairs of neighboring astrocytes from n=3 and 4 mice per
1099 group. **** = $p<0.0001$, Unpaired Welch`s T-test.

1100

1101 **Supplementary figure legends**

1102 **Fig S1. Astrocyte, neuron isolation and coculture from S1PR1-GFP reporter mice and WT**
1103 **mice respectively to study expression and function of S1PR1. (A)** Schematics of isolation and
1104 culture of astrocyte and neurons in vitro. **(B)** Purity of astrocyte cultures and expression of S1PR1-
1105 GFP (green) appears plasma membrane and stained with astrocyte marker S100b (red) in astrocyte
1106 only and A+N cocultures. **(C)** S1PR1-GFP expressing astrocytes showed two population of cells
1107 bright with complex morphology vs dim and roundish less complex cellular morphology.

1108

1109 **Fig S2. Astrocyte numbers as quantified by SOX9+ and Olig2- remain unchanged in**
1110 **S1PR1$^{\Delta AST}$ mice. (A)** Representative confocal 20x images stained with SOX9 (red) OLIG2
1111 (green) and Dapi (blue) from somatosensory cortices of **S1PR1$^{\Delta AST}$** or littermate control mice at
1112 P30. Boxed area is zoomed in and presented at the lower pannels. Arrowheads indicate
1113 SOX9+OLIG2- astrocytes. **(B)** Quantification of SOX9+OLIG2- astrocytes (left), SOX9+ cells
1114 (middle and OLIG2+ cells (right) represented as the cells/ 10,000μm^2 showing no changes in
1115 astrocyte numbers. Data represents the mean ± SEM of 19 and 19 images n=3 and 3 mice per
1116 group. n.s=non-significant, Unpaired Welch`s T-test.

1117

1118 **Fig S3. GFAP-Cre dependent GFP reporter mouse display minimal reporter expression in**
1119 **non-astrocytic cells. (A)** Schematics to show our breeding strategy to generate Cre dependent
1120 reporter mouse line by crossing our GFAP-Cre (no flox) with Lox-STOP-Lox-Cas9-P2A-GFP
1121 mouse line. **(B)** Representative confocal 20x images stained with GFP (green) and costained with
1122 either neuronal marker NeuN(red) (arrow indicates a NeuN+ GFP+ neuron), or microglial marker

1123 Iba1 (red), or Oligodendrocyte lineage marker OLIG2 (red) or **(C)** astrocyte marker GFAP (red)
1124 from P24 cortices or Hippocampus (only GFAP/GFP **(D)). (E)** Table with quantification of
1125 GFP+NeuN+, or GFP+Iba1+ or GFP+OLIG2+ cells as % of GFP labeled cells. Data represents
1126 the mean ± SEM of 9-11 images from n=3 mice.

1127

1128 **Fig S4. Membrane-targeted Lck-GFP labeled astrocytes from S1PR1$^{\Delta AST}$ mice exhibit**
1129 **complexity changes.** (**A**) Schematics showing AAV-based membrane labeling of **L2-3 astrocytes**
1130 *in vivo* by Lck-GFP. **(A-F) Sparsely labeled astrocytes from L2-3 somatosensory cortices were**
1131 **imaged and analyzed.** (**B**) Representative, confocal L2-3 membrane targeted-GFP filled
1132 astrocytes (left panel) and IMARIS rendered surface traces (right panels) **(C)** IMARIS rendered
1133 filament traces and astrocyte territory. **(D)** Quantification of astrocyte volume from Surface
1134 renderings generated using IMARIS. (**E**) Quantification of astrocyte territory volume (left) and
1135 filament length from filament traces generated using IMARIS. (**F**) Sholl analyses of IMARIS
1136 rendered filament traces of Lck-GFP labeled astrocytes from S1PR1$^{\Delta AST}$ and littermate controls.
1137 Data represents the mean ± SEM of 25-28 astrocytes from n=3 mice per group. * = $p<0.05$, ** =
1138 $p<0.01$, ns=non-significant, Unpaired Welch`s T-test. (**G-L**) **Sparsely labeled astrocytes from**
1139 **L4-5 somatosensory cortices were imaged and analyzed.** (**H**) Representative, confocal L4-5
1140 membrane targeted-GFP filled astrocytes (left panel) and IMARIS rendered surface traces (right
1141 panels) **(I)** IMARIS rendered filament traces and astrocyte territory. **(J)** Quantification of astrocyte
1142 volume from Surface renderings generated using IMARIS. (**K**) Quantification of astrocyte
1143 territory volume (left) and filament length from filament traces generated using IMARIS. (**L**) Sholl
1144 analyses of IMARIS rendered filament traces of Lck-GFP labeled astrocytes from S1PR1$^{\Delta AST}$ and

1145 littermate controls. Data represents the mean ± SEM of 27 and 37 astrocytes from n=3 mice per
1146 group. * = $p<0.05$, ** = $p<0.01$, **** = $p<0.0001$, ns=non-significant, Unpaired Welch`s T-test.

1147

1148 **Fig S5. Expression of Cre by AAV does not alter astrocytes morphology.** (**A**) Schematics
1149 showing delivery of AAV expressing GfaABC1D-YFP-P2A-Cre or GfaABC1D-YFP control in
1150 wildtype (WT) mouse pups. Sparsely labeled astrocytes were imaged from both upper and deeper
1151 somatosensory cortex from P30 pups. **(B)** Representative confocal images and subsequent
1152 IMARIS 3D surface/filament renderings of YFP astrocytes from control or Cre expressing
1153 littermates at P30. **(C)** Quantification of astrocyte volume (left) and soma volume (right) from
1154 Surface renderings generated using IMARIS. (**D**) Quantification of astrocyte territory volume from
1155 filament traces generated using IMARIS. (**E**) Sholl analyses of IMARIS rendered filament traces
1156 of astrocytes from Cre.P2A.YFP and YFP only. Data represents the mean ± SEM of 11 and 11
1157 astrocytes from n=3 mice per group. ns=non-significant, Unpaired Welch`s T-test.

1158

1159

Fig. 1

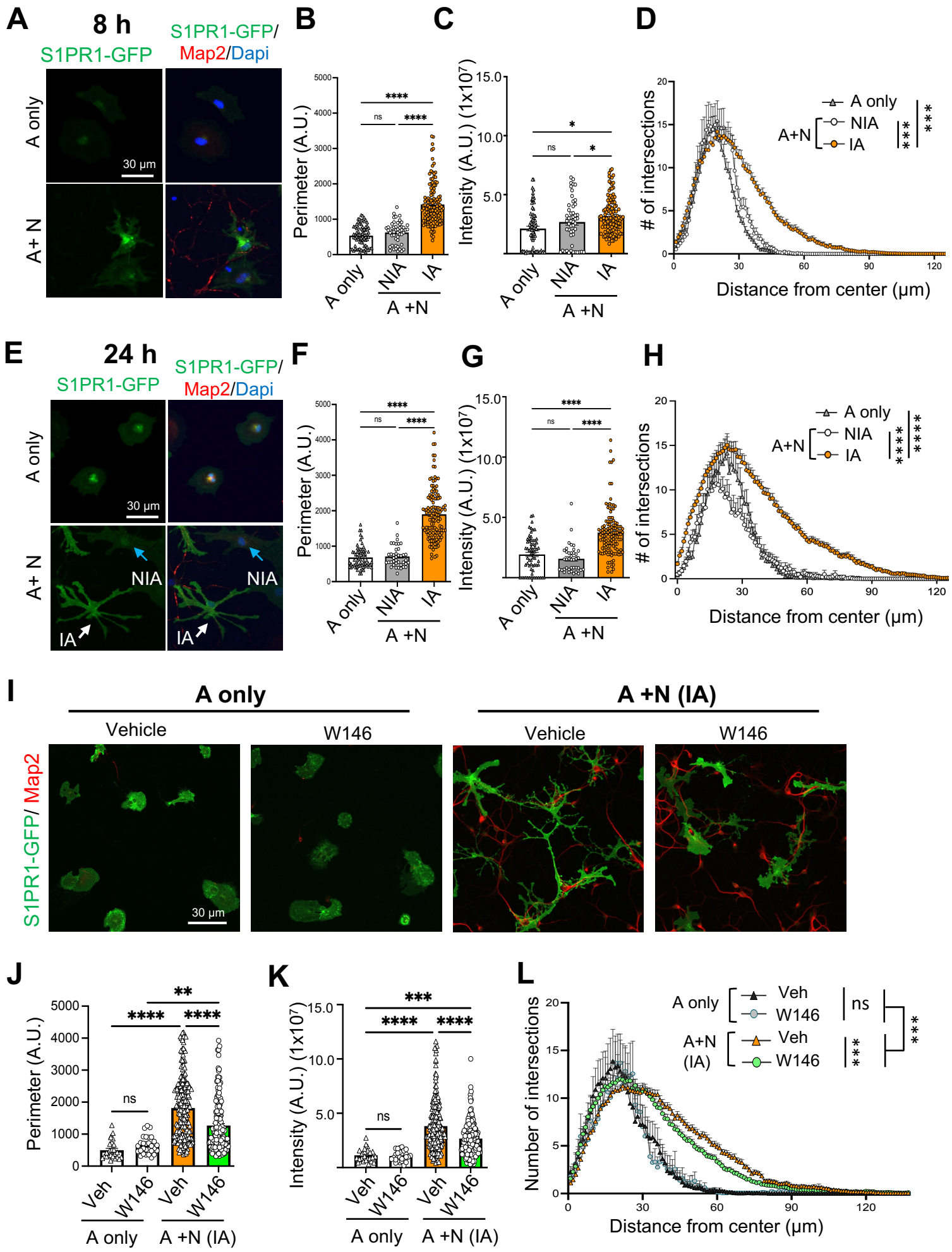
A
8 h
S1PR1-GFP
S1PR1-GFP/
Map2/Dapi
A only
A+ N
30 µm
B
Perimeter (A.U.)
****
ns
****
A only
NIA
IA
A +N
C
Intensity (A.U.) (1x10⁷)
*
ns
*
D
# of intersections
A only
A+N
NIA
IA
Distance from center (µm)
E
24 h
NIA
IA
F
G
H
I
A only
A +N (IA)
Vehicle
W146
S1PR1-GFP/ Map2
J
Veh
W146
K
L
Number of intersections
ns

Fig. 2

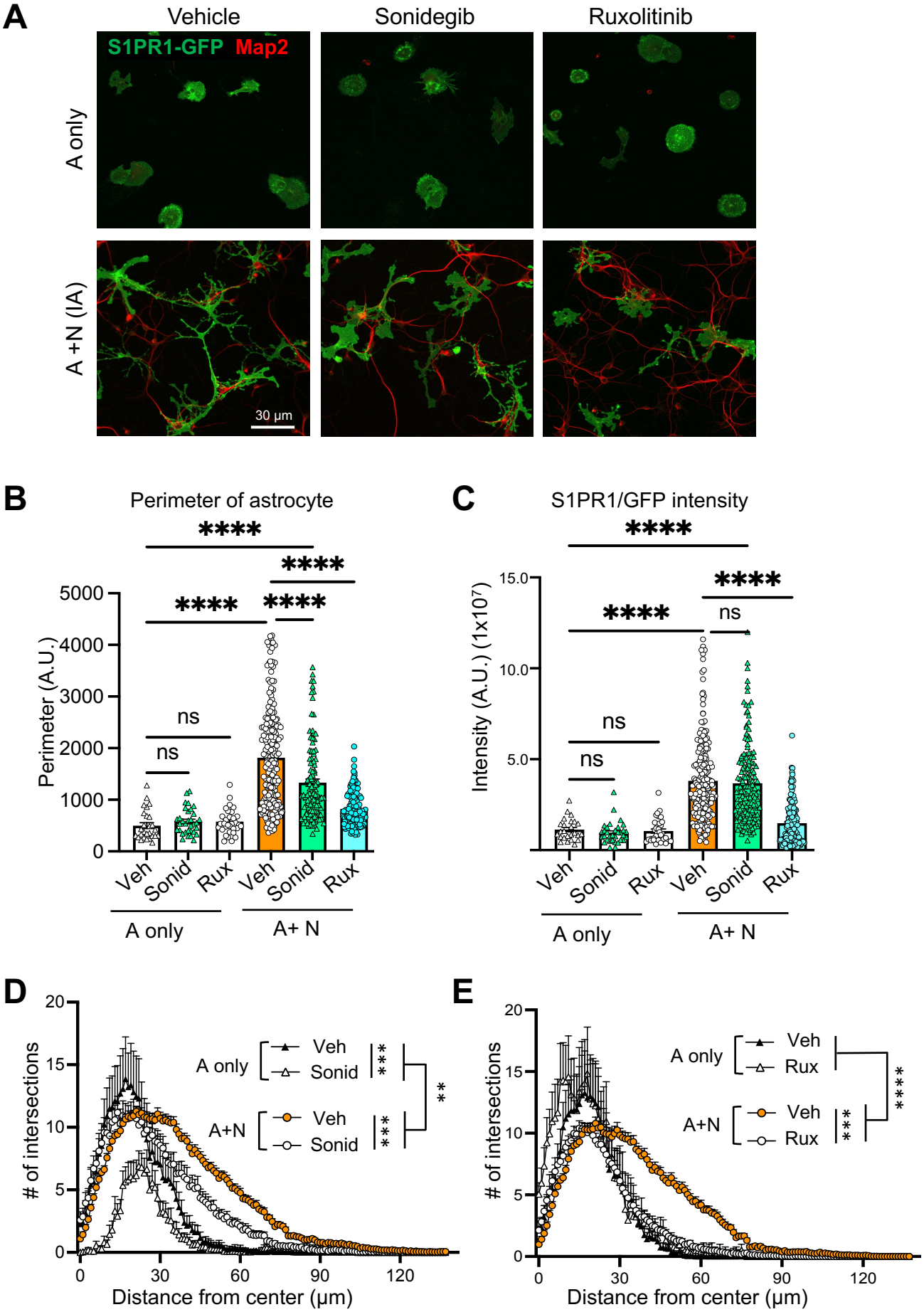
A
Vehicle
Sonidegib
Ruxolitinib
S1PR1-GFP Map2
A only
A +N (IA)
30 µm
B
Perimeter of astrocyte
Perimeter (A.U.)
5000
4000
3000
2000
1000
0
****
****
****
****
ns
ns
Veh
Sonid
Rux
Veh
Sonid
Rux
A only
A+ N
C
S1PR1/GFP intensity
Intensity (A.U.) (1x10^7)
15.0
10.0
5.0
****
****
****
ns
ns
ns
Veh
Sonid
Rux
Veh
Sonid
Rux
A only
A+ N
D
# of intersections
20
15
10
5
0
A only
Veh
Sonid
A+N
Veh
Sonid
***
***
**
0
30
60
90
120
Distance from center (µm)
E
# of intersections
20
15
10
5
0
A only
Veh
Rux
A+N
Veh
Rux
***
****
0
30
60
90
120
Distance from center (µm)

Fig. 3

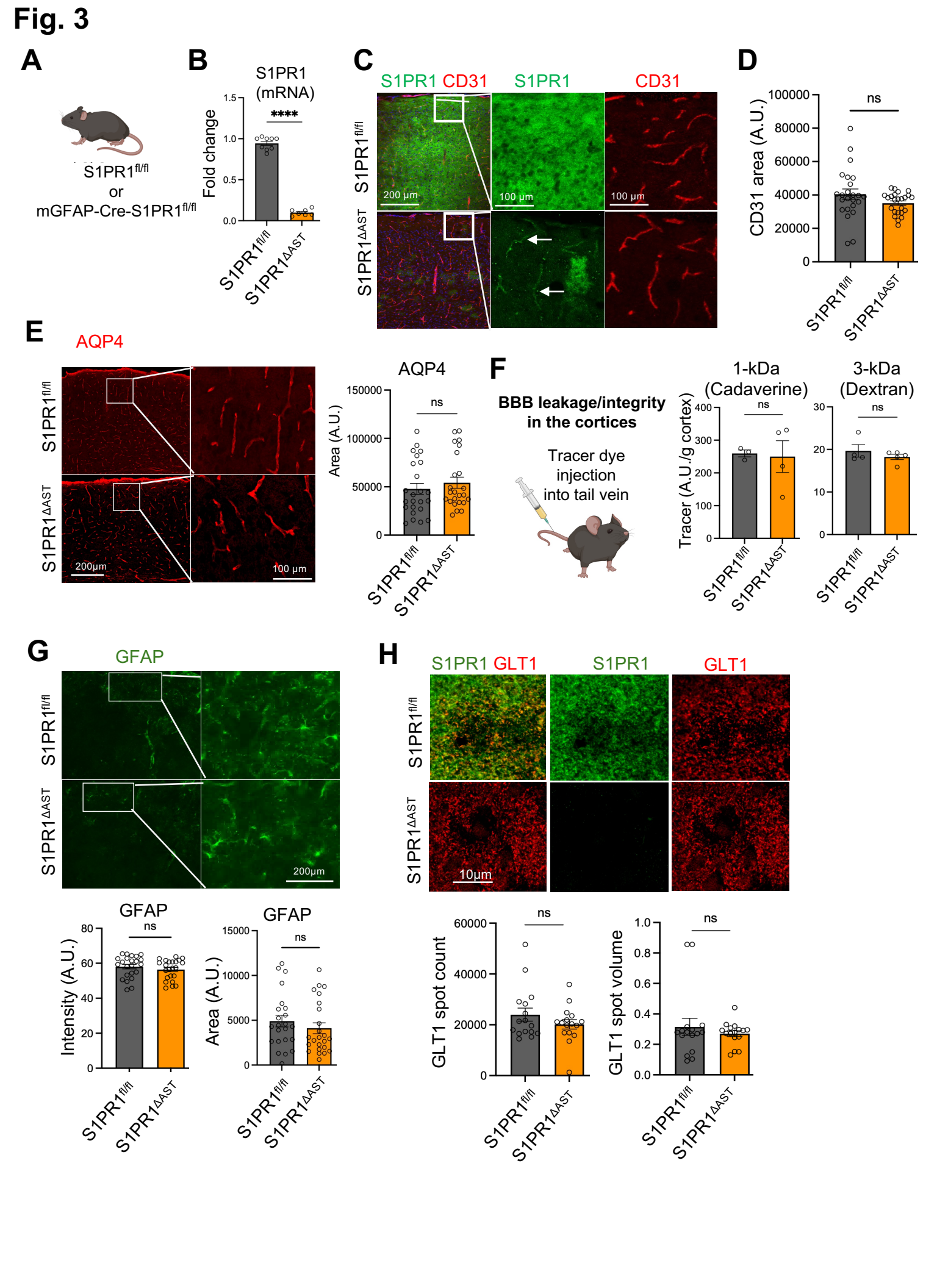
A
S1PR1fl/fl
or
mGFAP-Cre-S1PR1fl/fl
B
S1PR1 (mRNA)
Fold change
****
S1PR1fl/fl
S1PR1ΔAST
C
S1PR1 CD31
S1PR1
CD31
S1PR1fl/fl
S1PR1ΔAST
200 μm
100 μm
100 μm
D
CD31 area (A.U.)
ns
S1PR1fl/fl
S1PR1ΔAST
E
AQP4
S1PR1fl/fl
S1PR1ΔAST
200μm
100 μm
AQP4
Area (A.U.)
ns
S1PR1fl/fl
S1PR1ΔAST
F
BBB leakage/integrity in the cortices
Tracer dye injection into tail vein
1-kDa (Cadaverine)
3-kDa (Dextran)
Tracer (A.U./g cortex)
ns
ns
S1PR1fl/fl
S1PR1ΔAST
G
GFAP
S1PR1fl/fl
S1PR1ΔAST
200μm
GFAP
Intensity (A.U.)
ns
GFAP
Area (A.U.)
ns
S1PR1fl/fl
S1PR1ΔAST
H
S1PR1 GLT1
S1PR1
GLT1
S1PR1fl/fl
S1PR1ΔAST
10μm
GLT1 spot count
ns
GLT1 spot volume
ns
S1PR1fl/fl
S1PR1ΔAST

Fig. 4

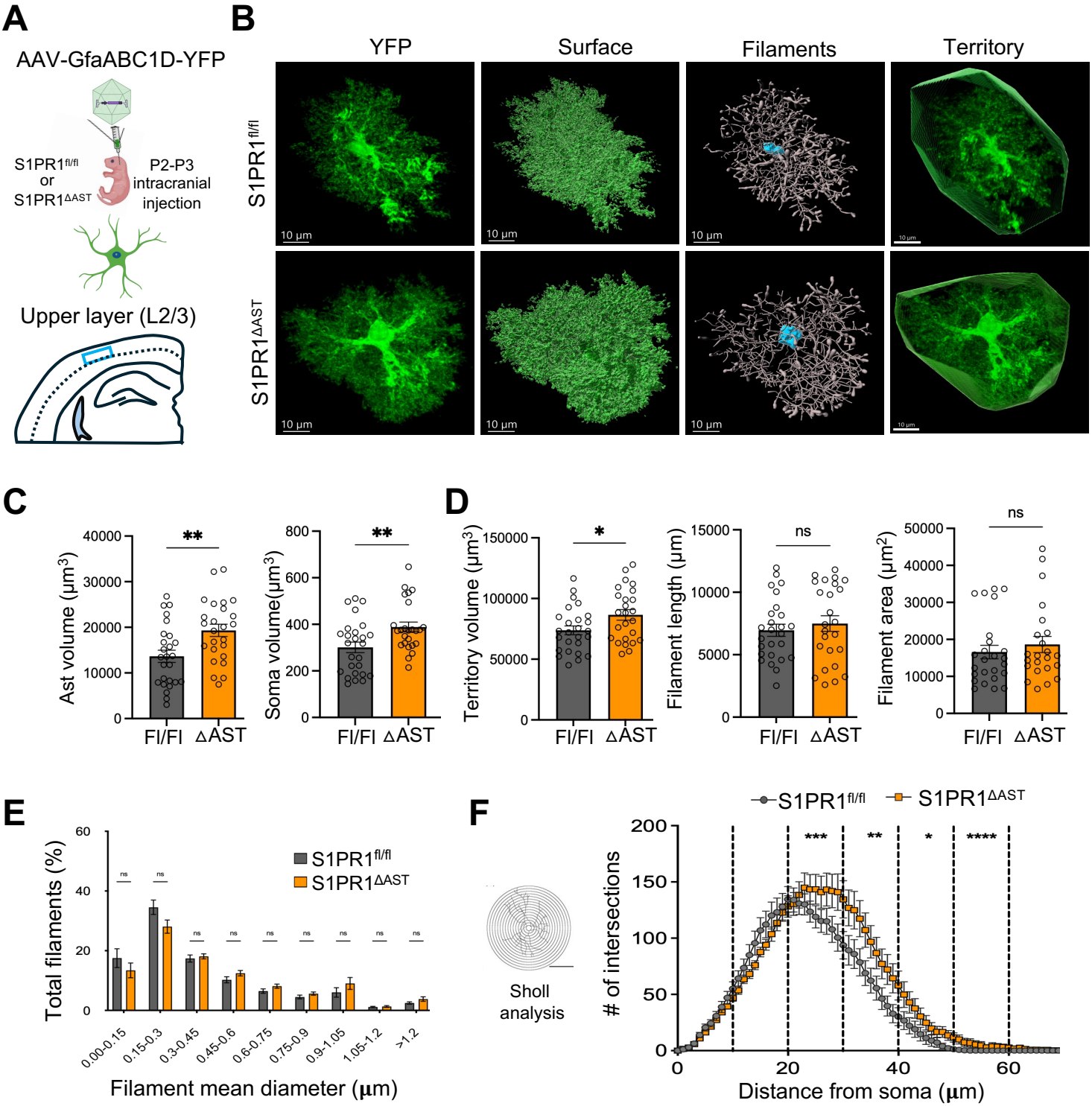
A
AAV-GfaABC1D-YFP
S1PR1fl/fl
or
S1PR1ΔAST
P2-P3
intracranial
injection
Upper layer (L2/3)
B
YFP
Surface
Filaments
Territory
S1PR1fl/fl
S1PR1ΔAST
10 µm
C
Ast volume (µm3)
Soma volume(µm3)
Fl/Fl
ΔAST
D
Territory volume (µm3)
Filament length (µm)
Filament area (µm2)
ns
E
Total filaments (%)
S1PR1fl/fl
S1PR1ΔAST
0.00-0.15
0.15-0.3
0.3-0.45
0.45-0.6
0.6-0.75
0.75-0.9
0.9-1.05
1.05-1.2
>1.2
Filament mean diameter (µm)
F
Sholl
analysis
# of intersections
Distance from soma (µm)

Fig. 5

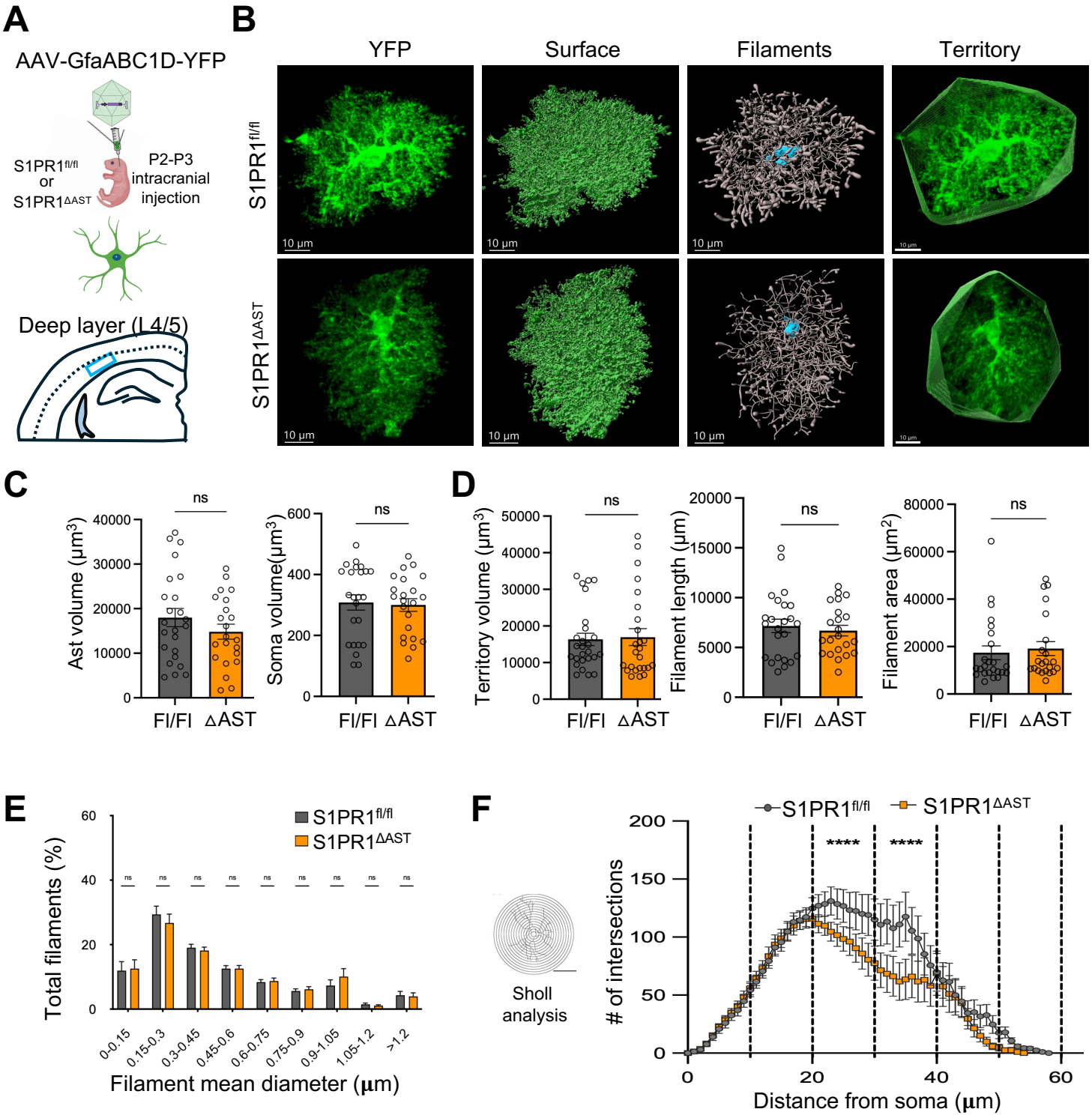
A
AAV-GfaABC1D-YFP
S1PR1fl/fl
or
S1PR1ΔAST
P2-P3
intracranial
injection
Deep layer (L4/5)
B
YFP
Surface
Filaments
Territory
S1PR1fl/fl
S1PR1ΔAST
10 µm
C
Ast volume (µm3)
Soma volume(µm3)
ns
Fl/Fl
ΔAST
D
Territory volume (µm3)
Filament length (µm)
Filament area (µm2)
E
Total filaments (%)
S1PR1fl/fl
S1PR1ΔAST
0-0.15
0.15-0.3
0.3-0.45
0.45-0.6
0.6-0.75
0.75-0.9
0.9-1.05
1.05-1.2
>1.2
Filament mean diameter (µm)
F
Sholl
analysis
# of intersections
Distance from soma (µm)
****

Fig. 6

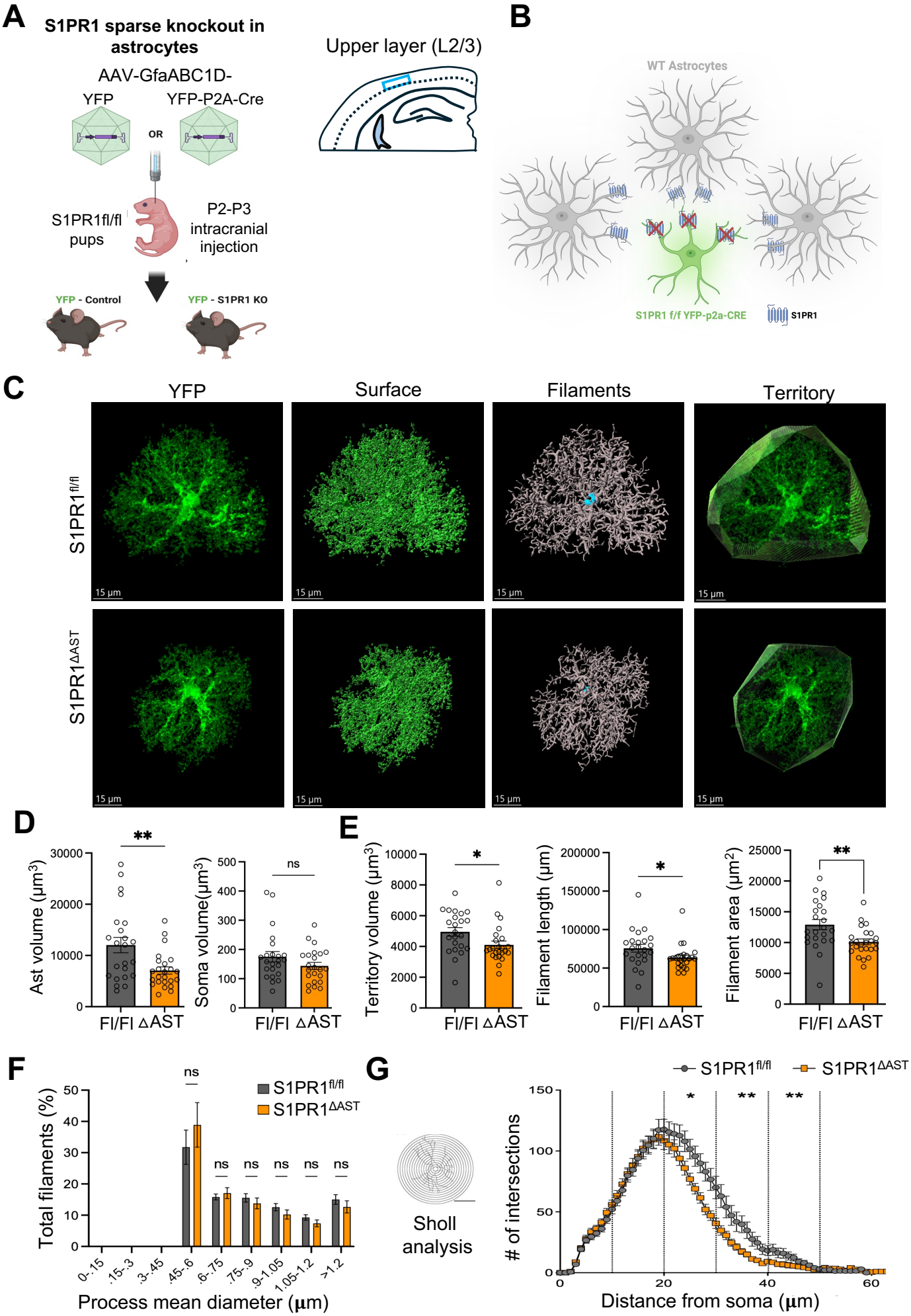
A
S1PR1 sparse knockout in astrocytes
AAV-GfaABC1D-
YFP
YFP-P2A-Cre
OR
S1PR1fl/fl pups
P2-P3 intracranial injection
YFP - Control
YFP - S1PR1 KO
Upper layer (L2/3)
B
WT Astrocytes
S1PR1 f/f YFP-p2a-CRE
S1PR1
C
YFP
Surface
Filaments
Territory
S1PR1fl/fl
S1PR1ΔAST
15 µm
D
Ast volume (µm3)
Soma volume(µm3)
Fl/Fl
ΔAST
ns
E
Territory volume (µm3)
Filament length (µm)
Filament area (µm2)
F
Total filaments (%)
Process mean diameter (µm)
0-.15
.15-.3
.3-.45
.45-.6
.6-.75
.75-.9
.9-1.05
1.05-1.2
>1.2
G
Sholl analysis
# of intersections
Distance from soma (µm)

Fig. 7

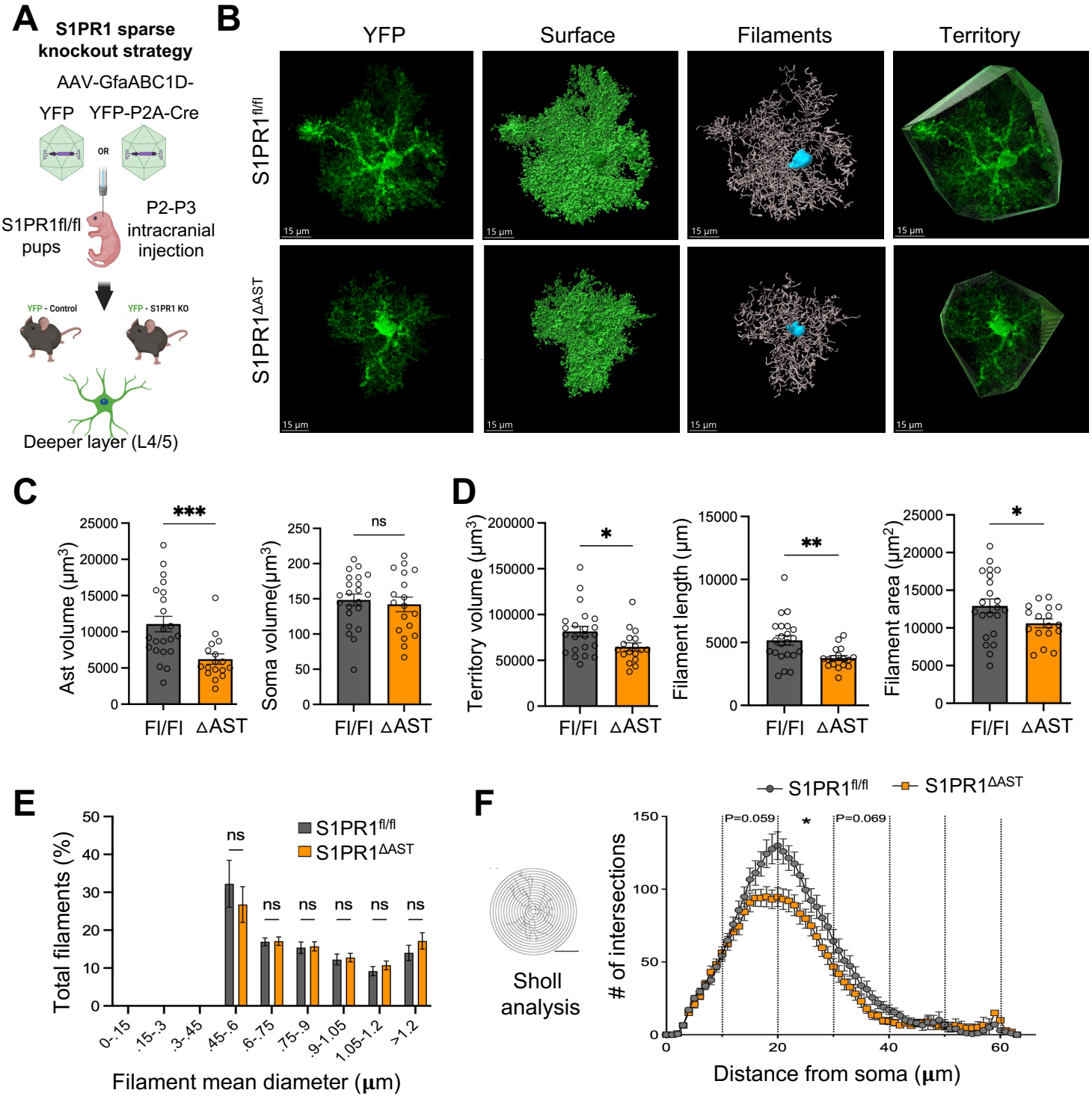
A
S1PR1 sparse knockout strategy
AAV-GfaABC1D-
YFP
YFP-P2A-Cre
OR
S1PR1fl/fl pups
P2-P3 intracranial injection
YFP - Control
YFP - S1PR1 KO
Deeper layer (L4/5)
B
YFP
Surface
Filaments
Territory
S1PR1fl/fl
S1PR1ΔAST
15 µm
C
Ast volume (µm3)
Soma volume(µm3)
***
ns
Fl/Fl
ΔAST
D
Territory volume (µm3)
Filament length (µm)
Filament area (µm2)
*
**
E
Total filaments (%)
S1PR1fl/fl
S1PR1ΔAST
ns
0-.15
.15-.3
.3-.45
.45-.6
.6-.75
.75-.9
.9-1.05
1.05-1.2
>1.2
Filament mean diameter (µm)
F
Sholl analysis
# of intersections
P=0.059
P=0.069
Distance from soma (µm)

Fig. 8

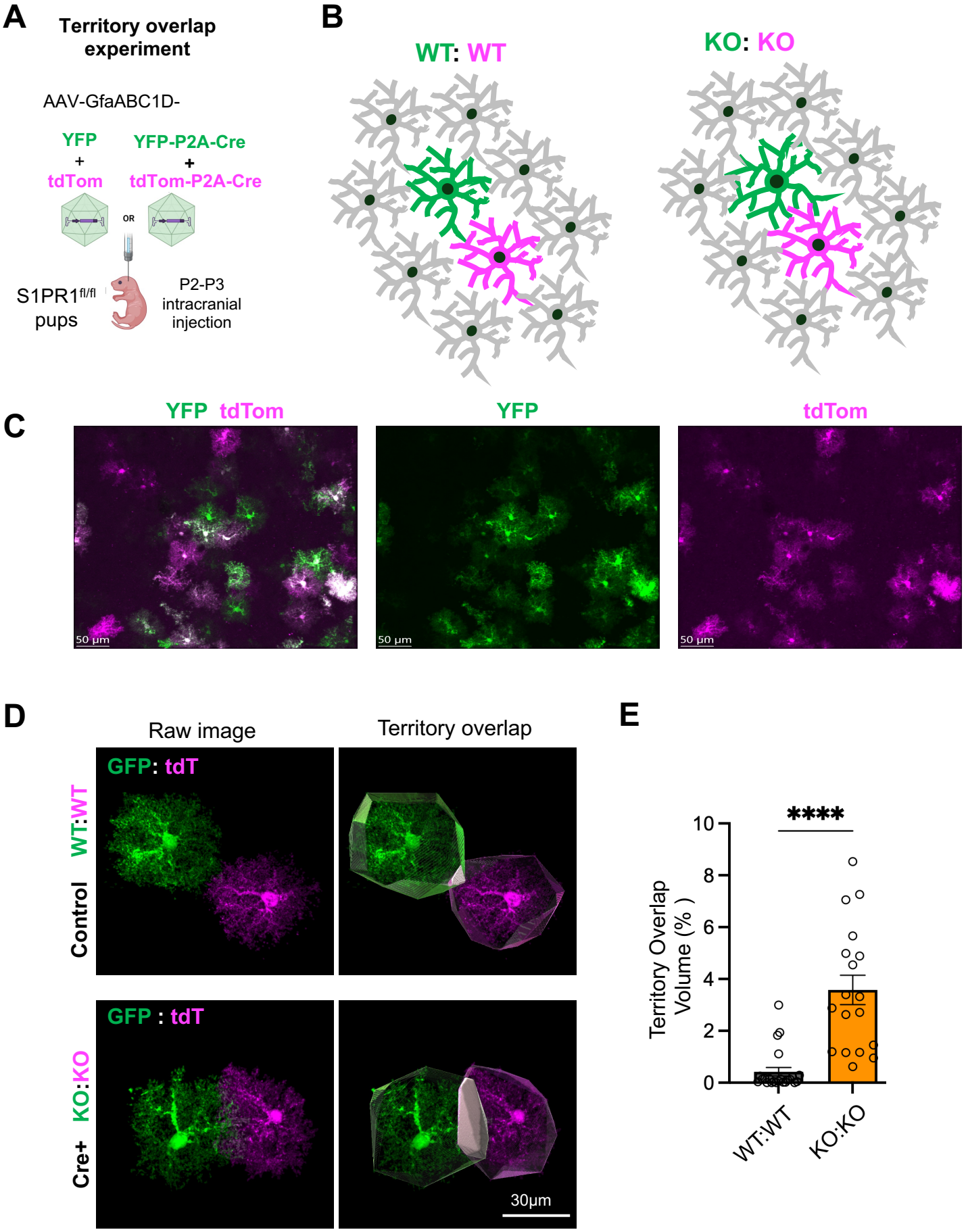
A
Territory overlap experiment
AAV-GfaABC1D-
YFP
+
tdTom
YFP-P2A-Cre
+
tdTom-P2A-Cre
OR
S1PR1fl/fl pups
P2-P3 intracranial injection
B
WT: WT
KO: KO
C
YFP tdTom
YFP
tdTom
50 µm
50 µm
50 µm
D
Raw image
Territory overlap
GFP: tdT
WT:WT
Control
GFP : tdT
KO:KO
Cre+
30µm
E
****
Territory Overlap Volume (%)
10
8
6
4
2
0
WT:WT
KO:KO